

In the format provided by the authors and unedited.

# Holocene dynamics of the Southern Hemisphere westerly winds and possible links to CO<sub>2</sub> outgassing

Krystyna M. Saunders<sup>1,2\*</sup>, Stephen J. Roberts<sup>3</sup>, Bianca Perren<sup>3</sup>, Christoph Butz<sup>1</sup>, Louise Sime<sup>3</sup>, Sarah Davies<sup>4</sup>, Wim Van Nieuwenhuyze<sup>5</sup>, Martin Grosjean<sup>1</sup> and Dominic A. Hodgson<sup>3,6</sup>

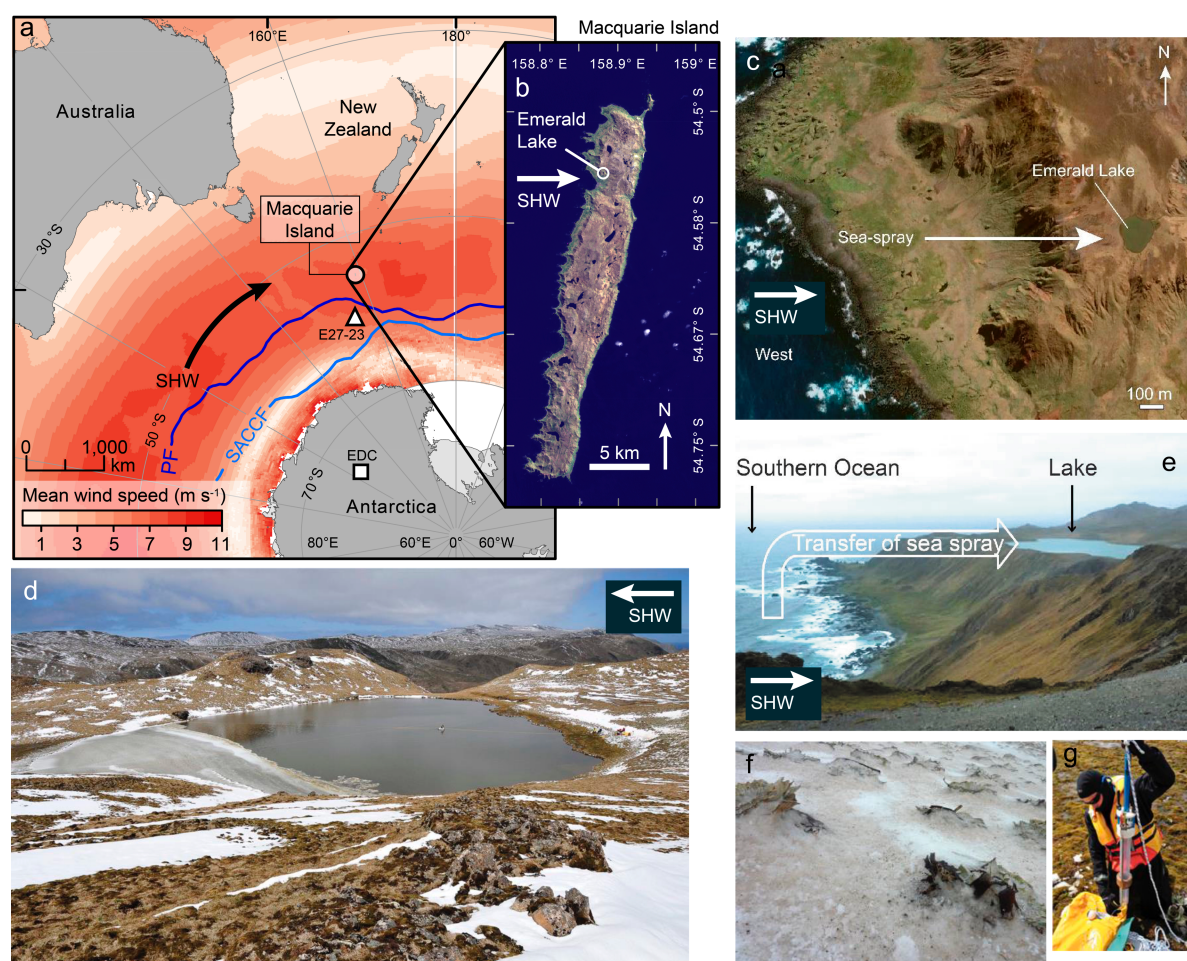
---

<sup>1</sup>Institute of Geography and Oeschger Centre for Climate Change Research, University of Bern, Bern, Switzerland. <sup>2</sup>Australian Nuclear Science and Technology Organisation, Sydney, Australia. <sup>3</sup>British Antarctic Survey, Cambridge, UK. <sup>4</sup>Department of Geography and Earth Sciences, Aberystwyth University, Aberystwyth, UK. <sup>5</sup>Department of Biology, University of Ghent, Ghent, Belgium. <sup>6</sup>Department of Geography, University of Durham, Durham, UK.  
\*e-mail: [krystyna.saunders@ansto.gov.au](mailto:krystyna.saunders@ansto.gov.au)

## Supplementary Information: Holocene dynamics of the Southern Hemisphere westerly winds and links to CO<sub>2</sub> outgassing

### Supplementary Note 1: Site selection, Macquarie Island

Macquarie Island (54°30'S, 158°57'E) is 34 x 5 km with an area of 120 km<sup>2</sup>. It is located 1500 km south-east of Tasmania, 1200 km south-west of New Zealand and 1300 km from the Antarctic continent (Supplementary Fig. 1). It is formed from oceanic crust uplifted as part of the Macquarie Ridge Complex, which runs south from New Zealand, emerging from about 600,000 years BP. Consequently, much of the island is composed of volcanic, sulphur-rich bedrock (primarily pillow basalts) and associated sediments<sup>1</sup>. The island consists of steep coastal slopes rising to a plateau at 200–300 m above sea level. Its highest point is 433 m. Landscape processes include faulting, tectonic uplift, sea level changes, erosion and periglacial activity. Widespread glaciation did not occur during the Last Glacial Maximum, although it is possible perennial ice and snow accumulated in some areas<sup>2</sup>. The island is extensively vegetated at lower altitudes with tussock grasslands, herbs and sedges, mosses, liverworts and lichens, and there are no tall shrubs or trees<sup>1</sup>. It has a cool oceanic climate with mean annual temperatures between 3.1 °C in winter and 6.6 °C in summer<sup>3</sup>, and winds are almost exclusively from the west (Supplementary Fig. 2a-e). Mean annual precipitation is 986.4 mm with rainfall on c. 316 days per year<sup>3</sup>.

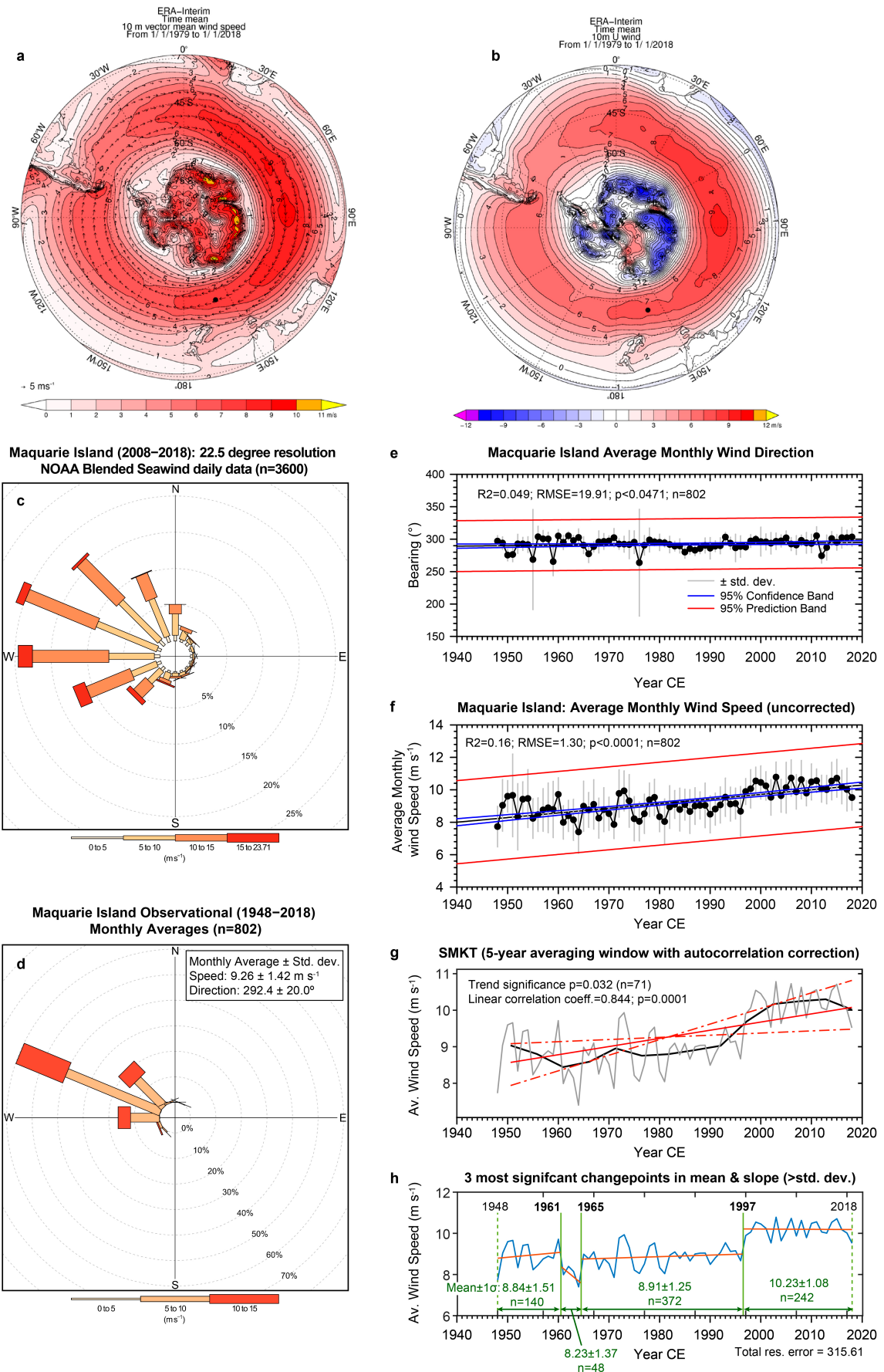


**Supplementary Figure 1. Location map and images of Macquarie Island and Emerald Lake.** **a, b.** Macquarie Island and mean Southern Ocean wind speed and Macquarie Island pansharpened LANDSAT8 satellite natural colour composite (pansharpened Bands 4,3,2). **c.** Emerald Lake. **d.** Emerald Lake during coring in 2013. **e.** West coast of Macquarie Island

where sea spray inputs result in a marked west to east gradient in lake conductivity of 1571–2  $\mu\text{S cm}^{-1}$  (ref. 27). **f.** Wind-blown particles deposited on snow covering the catchment after a windstorm in 2009. **g.** Surface sediment coring. The LANDSAT8 satellite image (bands 4,3,2) is courtesy of the U.S. Geological Survey (<https://earthexplorer.usgs.gov>). Mean annual wind-speeds shown in Figure 1a,b and in a are based on NOAA blended high resolution sea surface vector winds datasets, downloaded from (<https://www.ncdc.noaa.gov/data-access/marineocean-data/blended-global/blended-sea-winds>), and represent average annual surface-level (10 m) wind-speed, in a 0.25 degree grid between 1995–2005 CE (chosen because of its uniform seasonal distribution). Data were processed and converted to geotif rasters for ESRI ArcMap using R, courtesy of Alex Whittle (see Supplementary Note 8 for link to data). Annual mean wind speeds shown have errors of  $\pm 1 \text{ m s}^{-1}$  and are valid up to 10 m above the ocean surface. The image in Supplementary Figure 1c is © 2017 Google Earth (eye altitude = 1.51 km; centred on 54.546697S, 158.8735E).

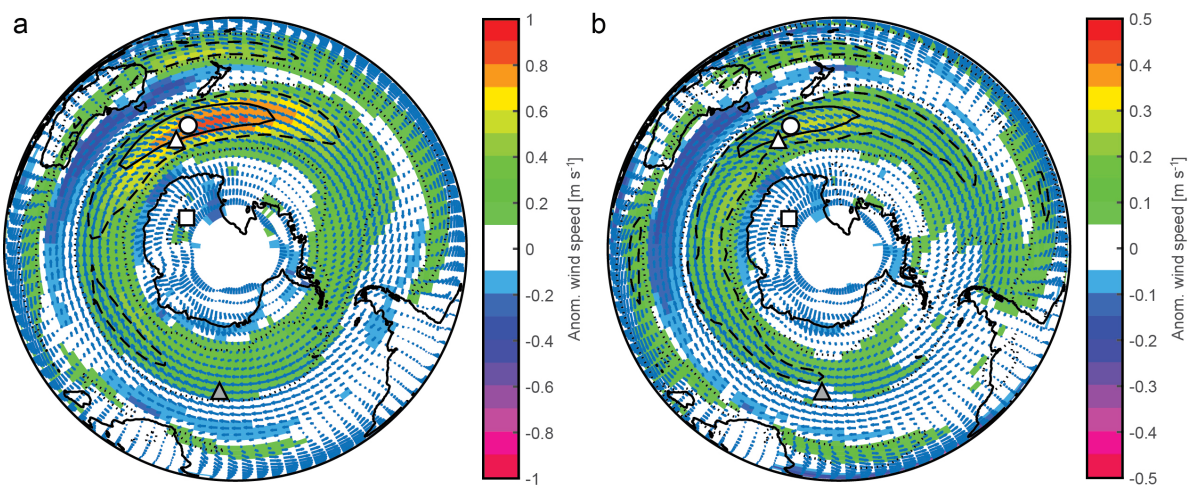
A significant upward trend in wind speed is evident in the Macquarie Island observational dataset since 1948 CE (after correction for serial autocorrelation in the time series). There has been no significant change in the wind-speed upward trend or in the prevailing wind-direction between 1948–2018 CE (Supplementary Fig. 2c-g). The three most significant changepoints in the monthly average wind-speed dataset (beyond the standard deviation of the mean and slope of the whole dataset) occurred in 1961, 1965, and 1997 CE. The most significant changepoint in the Macquarie Island wind-speed observational dataset occurred in 1997 CE (Supplementary Fig. 2h).

**Supplementary Figure 2 (overpage). Modern-day wind data for Macquarie Island.** **a, b.** Southern Hemisphere ERA-Interim global atmospheric reanalysis (1979–2018 CE). **c.** Wind-rose of daily surface ocean (10 m) vector wind-speed, wind-direction and wind-frequency at Macquarie Island (2008–2018 CE). **d.** Wind-rose of monthly wind-speed and wind-direction, and wind-frequency from observational measurements at the Macquarie Island Weather Station (1948–2018 CE). **e, f.** Average monthly wind-direction and wind-speed plots based on daily observational measurements at the Macquarie Island Weather Station (1948–2018 CE). **g.** Annual average of monthly wind-speed data (grey line), with 5-year average (black line) and Sequential Mann-Kendall Trend (SMKT) analysis (red line) applied to the Macquarie Island Weather Station data (1948–2018 CE). **h.** Changepoint analysis undertaken on average monthly wind-speed data from observational measurements at the Macquarie Island Weather Station (1948–2018 CE). Data shown in a and b are average annual 10 m all vector (U and V) and U (W-E) mean wind-speeds from 1/1/1979 to 1/1/2018 CE, and are similar to the NOAA 1995–2005 CE average blended wind-speed data shown in Figure 1a, b and Supplementary Figure 1 a. Macquarie Island is shown by the black circle. Data in c are daily wind-speed satellite derived wind-speed data from NOAA Blended Seawinds dataset for 2008–2018, centred on 158.93°E, 54.48 °S, the nearest grid square to the Macquarie Island base (see Supplementary Fig. 1a). Data in d, e, f are average monthly wind speed ( $\text{m s}^{-1}$ ), and bearing from four daily readings (at 0600, 1200, 1800, 0000 GMT) at 158.9°E, 54.5°S and 8 m a.s.l. between 1948–2018 CE (Australian Bureau of Meteorology data<sup>3</sup>, monthly averages were downloaded from <https://legacy.bas.ac.uk/met/READER/surface/stationwind.html>). See Supplementary Note 5, Supplementary Fig. 12 and Supplementary Table 8 for details of the SMKT and changepoint analysis, which are shown in g and h, respectively. In h, mean $\pm$ std. dev. and number of datapoints (n) for each changepoint zone are shown in green.



Supplementary Figure 2 (caption previous page)

The coupled climate modelling (Fig. 1c, d and reproduced in Supplementary Fig. 3) was used to assess the representativeness of Macquarie Island as a site for reconstructing the Southern Hemisphere westerly winds (SHW). We examined annual means and decadal data from a 300 year long pre-industrial simulation in the HadCM3 coupled model. The simulation was first presented in ref <sup>4</sup> and is used here to test how representative the top 20% of highest wind speed events at Macquarie Island are of Southern Hemisphere wind speeds. This analysis shows that SHW changes recorded at Macquarie Island are representative of changes, both at the annual (Supplementary Fig. 3a) and decadal (Supplementary Fig. 3b) time-scale around the whole of the Southern Ocean. Strongest changes occur in the southwestern Pacific. There is some weakening north of 50°S and around New Zealand and Southern Australia. These results suggest that measured wind changes at Macquarie Island provide a reliable proxy for SHW wind changes in their core belt in the Southeast Indian Ocean to the South Pacific sectors.



**Supplementary Figure 3. Southern Hemisphere wind speed anomalies associated with the top 20% of highest wind-speed events at Macquarie Island.** **a.** Annual mean. **b.** Decadal, filtered using a 11-year running mean prior to calculations. Macquarie Island is marked with a white circle, the EPICA Dome C (EDC) ice core with a white square, and the Southern Ocean winter sea ice extent from marine cores PS2090 with a grey triangle and E27-23 with a white triangle. Dashed (solid) black contours show the 0.5 (0.75) correlations associated between Macquarie Island wind changes and changes in wind elsewhere in the Southern Hemisphere.

#### Supplementary Note 2: Site selection, Emerald Lake

Emerald Lake ( $54^{\circ}40'22''\text{S}$ ,  $158^{\circ}52'14''\text{E}$ ) is a small, shallow polymictic, oligotrophic freshwater lake (approximately  $130 \times 120$  m with a maximum depth of 1.2 m). It is situated 170 m above sea level on the north-western edge of the Macquarie Island plateau. It is 900 m from the coast, and directly exposed to the SHW (Supplementary Fig. 1b,c). The lake has an area of c.  $9,800 \text{ m}^2$  and a small catchment to lake ratio of c. 4:1 (Supplementary Fig. 1d). There are two small seepage outflows above the current lake water level, which were inactive at the time of sampling. A higher former lake level is evident on W/NW side, approximately 50 cm higher than the current lake level, which could have reactivated the outflow on the southern side of the lake. The island has experienced some impacts from non-indigenous species including rabbits since the late 1800's CE, but these have now been removed following an eradication programme in 2010–2013<sup>5</sup>. As with all lakes on the island, sea spray is the principal source of sea salt ions, with geochemical weathering playing a

minor role<sup>6</sup>. Minerogenic aerosols have also been observed in the catchment following high wind events (Supplementary Fig. 1e,f).

### Supplementary Note 3: Emerald Lake sediment coring, and geochronology

Lake sediment cores were collected from the deepest part of the lake using a combination of Glew gravity, UWITEC and Livingstone corers. An intact mastercore for scanning (micro-XRF,  $\mu$ -XRF, and hyperspectral imaging, Specim) consisted of two drives (EL13: LIV1A and LIV1C), combined at fixed depths of 73 and 83 cm, with a maximum composite depth of 111 cm. Core sections were aligned using Analyseries software and a combination of field depth measurements, visual stratigraphy, diatoms, total organic carbon (TOC), total sulphur (TS)<sup>5</sup>, magnetic susceptibility and  $\mu$ -XRF data.

We established two independent downcore chronologies for cores extracted from Emerald Lake between 2006–2010 CE (EL06/09/10), and in 2013 (EL13). Chronologies for the lake sediment cores were established using 35 Accelerator Mass Spectrometry (AMS) radiocarbon ( $^{14}\text{C}$ ) ages. We dated the following material in order of preference: 1) identifiable plant macrofossil remains; 2) terrestrial and/or lacustrine algae; 3) other intact macrofossils and sub-fossils, including woody fragments; 4) organic-rich bulk sediments and, near the base of each core 6) bulk sediments. Bulk sediments were only dated where macrofossils were absent.

Lead isotope (Pb-210) ages were also included in the EL06/09/10 age-depth model shown in Supplementary Figure 6a. EL06/09/10 cores were sliced in the lab or field providing a sub-sample-only diatom-inferred conductivity record (Supplementary Fig. 6a), while EL13 cores were retained intact and were used primarily for multi-sensor core logging (MSCL-GEOTEK),  $\mu$ -XRF (ITRAX™) and hyperspectral (Specim Ltd.) scanning analysis (Supplementary Fig. 6b). Samples were sent to ANSTO (Australia), Rafter Radiocarbon (New Zealand) and Beta Analytic (USA) for dating analysis.

Macrofossils from the EL13 cores were hand-picked from frozen bulk material after overnight defrosting at 5 °C, immersed in ultra-pure (18.2 MΩ) water, sealed and placed in an ultrasonic bath for an hour, sieved to remove fine particles, picked under a binocular microscope and dried/refrozen. Macrofossils dated at Beta Analytic were acid washed, while bulk sediment samples were leached with a 0.5 M to 1.0 M HCl bath to remove carbonates and heated to 70 °C for 4 hours. Leaching was repeated until no carbonate remained, followed by rinsing to neutral 20 times with deionised water, placed in 0.5% to 2% solution of NaOH for 4 hours at 70 °C and rinsed to neutral 20 times with deionised water. The process was repeated until no additional reaction (typically indicated by a colour change in the NaOH liquid) was observed. Samples were then leached again in a 0.5 M to 1.0 M HCl bath to remove any CO<sub>2</sub> absorbed from the atmosphere by the NaOH soakings and to ensure initial carbonate removal was complete, and then dried at 70 °C in a gravity oven for 8–12 hours.

Radiocarbon age data are reported as conventional radiocarbon years BP ( $^{14}\text{C}$  years BP)  $\pm 1\sigma$ , and as two-sigma (2 $\sigma$ , 95.4%, unless stated) calibrated age ranges (cal yr BP), mean  $\pm 1\sigma$ , and median calibrated ages (cal. a BP, relative to 1950 CE) (Supplementary Table 2). Measured radiocarbon ages from samples shown in Supplementary Table 2 were calibrated in OXCAL v4.2<sup>7</sup> using the SH13 terrestrial and post-bomb calibration curves<sup>8,9</sup>. Post-bomb (>1950 CE) samples were corrected according to  $^{13}\text{C}/^{12}\text{C}$  isotopic ratios from measured pMC, where the ‘present day’ pMC value is defined as 107.5% (2010 CE), and calibrated using the SHCal13 SH Zone 1-2 Bomb curve using CALIBOMB<sup>10,11</sup>. Calibrated age data in Supplementary Table 2 were rounded to the nearest 5 years where measured radiocarbon age errors were less than  $\pm 50$  radiocarbon years and

to the nearest 10 years where measured radiocarbon age errors were greater than  $\pm 50$  radiocarbon years. Unlike Saunders et al. (2013), we did not apply a small lake reservoir offset of  $198\pm30$   $^{14}\text{C}$  years to bulk sediment radiocarbon ages. When calibrated,  $198\pm30$   $^{14}\text{C}$  years has a ‘modern’ upper calibrated age range (95.4% error), and overlaps with Pb-210 ages from the uppermost rabbit-influenced lithological unit <sup>5</sup> (labelled R in Supplementary Fig. 6; Supplementary Tables 1, 2).

Macrofossils extracted from near the surface of the EL13 core also returned modern, ‘post-bomb’ (<1950 CE) ages (Supplementary Table 2). While the Saunders et al. (2013) Pb-210 produced a robust chronostratigraphy for the EL06 surface core used in the conductivity record, comparison with radiocarbon dated bulk surface sediments to establish a potential lake reservoir effect on Macquarie Island is complicated by the flocculent nature of the uppermost rabbit-influenced unit. The introduction of rabbits is well-defined by significant changes in diatom stratigraphy and geochemistry at c. 20 cm in the conductivity record, and at c. 16–17 cm depth in the scanning record, and, therefore, we use this precise marker horizon of c. 1903 CE to link the base of the uppermost units in the two age-depth models. The EL13 mastercore below 73 cm is used in both the conductivity and scanning records. We also included additional radiocarbon age data from below 73 cm depth from the EL09 core after realignment with the EL13 mastercore. Realignment was undertaken in Analyseries based on the strong correlation between EL09 sub-sample TOC data and EL13 inc/coh  $\mu$ -XRF ratios (Before:  $r^2=-0.24$ ; after:  $r^2=0.77$ ), and S determined from sub-sample and  $\mu$ -XRF analysis (Before:  $r^2=0.23$ ; after:  $r^2=0.81$ ).

Age-depth models were generated using the Bayesian age-depth modelling program BACON v2.2 in R <sup>12,13</sup>, with ‘as measured’ (uncalibrated) radiocarbon age data shown in Supplementary Table 1 used as input data (Supplementary Fig. 6). Bayesian accumulation histories were reconstructed in 1 cm segments progressively upcore by combining calibrated radiocarbon ages with ‘prior’ information. Prior settings for the EL13 age-depth models runs were: acc. shape = 1.5, acc. mean = 100 a  $\text{cm}^{-1}$ , mem. strength = 20, mem. mean = 0.1, segment thickness = 1 cm (Supplementary Fig. 6). Additional priors were included at zero depth to prevent the age-depth models overrunning into the future (EL06-10: 0 cm=2006 CE; EL13: 0 cm=2013 CE). All data in each mastercore, including outliers that created unfeasible age-depth reversals (e.g., at 109.5 cm depth), were included in the age-depth modelling. Incompatible ages were excluded as the program ran several million Markov Chain Monte Carlo Bayesian age-depth modelling simulations by estimating the accumulation rate in each 1 cm segment and how it relates to the 1 cm section above. The effect of various segment thickness and mean accumulation rates were tested. Apart from reducing the segment thickness from 5 cm to 1 cm, varying the default prior settings had no significant effect on the overall age-depth profiles produced. Similarly, there was no significant difference in age-depth model outputs when using the 95% or 5% probability post-bomb calibrated ages. Modelled ages quoted in the text were derived from the ‘best-fit’ (weighted mean) age of the BACON age depth model (red lines in Supplementary Fig. 6) and have been rounded to the nearest 10 years, with minimum to maximum 95% confidence ages shown in square brackets. Rounding to the closest 100-years better reflects the level of precision achievable for ages outside the period dated by Pb-210, i.e., plots of sub-mm and sub-cm proxy data at annual and sub-annual resolution does not imply that this level of radiocarbon dating precision is realistic.

**Supplementary Table 1. Radiocarbon data from conductivity and scanning mastercores from Emerald Lake used in this study.**

ID no.	Lab. ID	Core_section_ID	Core	Mastercore	Material dated	$\delta^{13}\text{C}$ (‰) ± 0.1 (1σ)	Measured $^{14}\text{C}$ age ( $^{14}\text{C}$ a BP)	SH13 Calibrated Ages (cal. a BP)		
			Depth (cm)	Depth (cm)				95.4% range	Median	Mean ± 1σ
<b>a) Emerald Lake: Conductivity Mastercore only</b>										
1	NZA 28449	EL06_0-1	0	0.5	Bulk organic sediment	-24.4	$198 \pm 30$	290 – –	185	$175 \pm 75$
2	NZA 35297	EL09_1A_2	7	7.0	Plant macrofossil	-29.1	$185 \pm 15$	285 – –	210	$185 \pm 80$
3	NZA29115	EL06_22	22	22.0	Bulk organic sediment	-24.9	$2,873 \pm 20$	3,030 – 2,850	2,930	$2,935 \pm 45$
4	OZL585	E 27.5-28	27	27.0	Bulk organic sediment	-23.2	$4,080 \pm 50$	4,815 – 4,405	4,520	$4,545 \pm 105$
5	OZL586	E 37-37.5	37	37.0	Bulk organic sediment	-23.4	$4,825 \pm 50$	5,610 – 5,325	5,515	$5,500 \pm 75$
6	NZA 50563	EL10_1B_88	43.5	49.3	Bulk organic sediment	-28.1	$7,143 \pm 31$	8,000 – 7,845	7,935	$7,925 \pm 40$
7	NZA 28451	EL06_50	50	50.0	Bulk organic sediment	-25.1	$6,306 \pm 40$	7,275 – 7,015	7,200	$7,185 \pm 65$
8	NZA 50564	EL10_1B_117	58	64.0	Bulk organic sediment	-29.4	$6,883 \pm 30$	7,750 – 7,590	7,670	$7,670 \pm 40$
9	Beta-329657	EL10_1B_131	65	71.0	Bulk organic sediment	-27.1	$6,990 \pm 50$	7,930 – 7,675	7,780	$7,780 \pm 65$
<b>b) Emerald Lake: Scanning Mastercore only</b>										
10	Beta-437013	EL13-1A-10	10	10.0	Plant macrofossil	-27.6	$100.4 \pm 0.3$ pMC	-7.42 – -5.04*	-	$-6 \pm 1$
- Rabbit Zone Correlation (diatom-based)			16	16.0	-	-	-	-57 – -37	-47	$-47 \pm 10$
11	Beta-437014	EL13-1A-16	16	16.1	Plant macrofossil	-26.1	$160 \pm 30$	280 – –	110	$130 \pm 85$
12	Beta-443812	EL13-1A-17	17	17.0	Wood macrofossil	-29.0	$106.3 \pm 0.3$ pMC	-60.9 – -55.3*	-	$-58 \pm 3$
13	Beta-443813	EL13-1A-20	20	20.0	Bulk Organic sediment	-23.8	$4,230 \pm 30$	4,845 – 4,580	4,725	$4,720 \pm 70$
14	Beta-437015	EL13-1A-23.5	23.5	23.5	Plant macrofossil	-28.7	$4,690 \pm 30$	5,570 – 5,305	5,405	$5,400 \pm 55$
15	Beta-437016	EL13-1A-28	28	28.0	Plant macrofossil	-26.0	$5,980 \pm 30$	6,880 – 6,665	6,760	$6,765 \pm 50$
16	Beta-437017	EL13-1A-33	33	33.0	Plant macrofossil	-25.2	$6,240 \pm 40$	7,250 – 6,980	7,090	$7,095 \pm 70$
17	Beta-437018	EL13-1A-37	37	37.0	Plant macrofossil	-29.3	$6,560 \pm 40$	7,555 – 7,320	7,435	$7,430 \pm 50$
18	Beta-437019	EL13-1A-47.5	47.5	47.5	Plant macrofossil	-27.6	$6,640 \pm 40$	7,570 – 7,430	7,495	$7,495 \pm 40$
19	Beta-437020	EL13-1A-62	62	62.0	Bulk Organic sediment	-30.3	$7,060 \pm 30$	7,940 – 7,755	7,860	$7,860 \pm 50$
<b>c) Emerald Lake: Conductivity and Scanning Mastercore</b>										
20	Beta-380671	EL13-1C 53.4-53.8	53.4	76.40	Bulk organic sediment	-28.3	$7,500 \pm 30$	8,365 – 8,190	8,275	$8,275 \pm 50$
21	NZA 50567	EL09_2B_115	57	83.35	Bulk organic sediment	-28.8	$7,925 \pm 33$	8,975 – 8,585	8,685	$8,705 \pm 90$
22	Beta-382320	EL13-1C 62.6-62.8	62.6	85.60	Bulk organic sediment	-26.2	$8,510 \pm 30$	9,535 – 9,440	9,490	$9,490 \pm 25$
23	NZA 35298	EL09_2B_65-65.5	65	87.05	Bulk organic sediment	-27.5	$9,301 \pm 25$	10,555 – 10,290	10,440	$10,430 \pm 70$
24	Beta-329654	EL09_2B_135	67	89.48	Bulk organic sediment	-27.9	$9,510 \pm 60$	11,085 – 10,555	10,725	$10,770 \pm 150$
25	Beta-382321	EL13-1C 69.8-70	69.8	92.80	Bulk organic sediment	-29.1	$9,560 \pm 30$	11,080 – 10,680	10,835	$10,870 \pm 130$
26	Beta-357226	EL09_2B_137	68	93.28	Bulk organic sediment	-27.4	$9,580 \pm 40$	11,090 – 10,695	10,890	$10,895 \pm 120$
27	Beta-382321	EL13-1C 72.6-73	72.6	95.60	Bulk organic sediment	-27.6	$9,770 \pm 30$	11,235 – 10,905	11,180	$11,165 \pm 60$
28	Beta-357227	EL09_2B_140	69.5	97.33	Bulk organic sediment	-28.6	$9,690 \pm 40$	11,200 – 10,785	11,010	$11,005 \pm 125$
29	Beta-382322	EL13-1C 74.6-74.8	74.6	97.60	Bulk organic sediment	-28.2	$9,790 \pm 30$	11,240 – 11,120	11,195	$11,185 \pm 40$
30	NZA 50632	EL09_2B_141	70	97.62	Bulk minerogenic sediment	-34.8	$13,659 \pm 56$	16,660 – 16,190	16,410	$16,420 \pm 120$
31	NZA 35320	EL09_2B_29/basal	75.5	108.68	Bulk minerogenic sediment	-25.5	$7,902 \pm 35$	8,950 – 8,540	8,645	$8,665 \pm 80$
32	Beta-329655	EL09_2B_156/basal	77.5	109.32	Bulk minerogenic sediment	-26.3	$8,670 \pm 50$	9,735 – 9,500	9,595	$9,605 \pm 60$
33	Beta-380675	EL13-1C 86.5/basal	86.5	109.50	Bulk minerogenic sediment	-25.0	$7,030 \pm 30$	7,935 – 7,715	7,825	$7,825 \pm 55$
34	Beta-357228	EL09_2B_158/basal	78.5	109.67	Bulk minerogenic sediment	-24.8	$8,620 \pm 40$	9,660 – 9,480	9,540	$9,545 \pm 40$

Continued overpage

ID no.	Lab. ID	Core_section_ID	Core	Mastercore	Material dated	$\delta^{13}\text{C}$ (‰) ± 0.1 (1 $\sigma$ )	Measured $^{14}\text{C}$ age ( $^{14}\text{C}$ a BP)	SH13 Calibrated Ages (cal. a BP)		
			Depth (cm)	Depth (cm)				95.4% range	Median	Mean ± 1 $\sigma$
d) Emerald Palaeolake data										
35 Beta-382317	EL-PL4_49-50	49.5	-	Plant macrofossil	-27.5	9,230 ± 40	10,495 – 10,240	10,345	10,350 ± 70	
e) Data not included in final mastercores (EL09-1A and EL09-2B<73 cm & EL10_1B<50 cm & >73 cm)										
36 NZA 50682	EL10_1B_45	22	29.2	Bulk organic sediment	-30.0	6,314 ± 57	7,320 – 7,000	7,200	7,190 ± 85	
37 Beta-329656	EL10_1B_60	29.5	35.3	Bulk organic sediment	-29.0	4,470 ± 40	5,285 – 4,865	5,025	5,055 ± 120	
38 NZA 35300	EL09_1A_11	35.3	35.3	Plant macrofossil	-28.7	6,344 ± 20	7,280 – 7,165	7,225	7,225 ± 35	
39 NZA 35302	EL09_2B_20b	16.5	36.1	Wood	-29.3	6,628 ± 20	7,565 – 7,430	7,480	7,485 ± 35	
40 NZA 35299	EL09_1A_16	55.3	55.3	Plant macrofossil	-30.6	6,219 ± 20	7,170 – 6,985	7,080	7,080 ± 50	
41 NZA 50565	EL09_2B_67	33	56.8	Bulk organic sediment	-31.7	9,317 ± 37	10,575 – 10,290	10,455	10,450 ± 75	
42 NZA 35301	EL09_2B_24	44.5	69.2	Wood	-30.2	7,591 ± 20	8,410 – 8,330	8,375	8,370 ± 25	
43 NZA 50566	EL09_2B_103	51	72.5	Bulk organic sediment	-29.6	8,028 ± 33	9,005 – 8,655	8,865	8,855 ± 90	
44 NZA 50683	EL10_1B_145	72	78.0	Bulk organic sediment	-28.8	8,071 ± 67	9,095 – 8,640	8,890	8,880 ± 120	

Notes: The sample codes refer to the core, year of collection, core half used, sample no. (EL06-09-10 cores were sub-sampled at 0.5 cm intervals). EL06 and EL10\_1B are Glew and UWITEC surface core respectively; EL09\_2B and EL13\_1A/1C were Livingston cores. This table includes all radiocarbon data in Saunders et al. (2013) and is supplemented by EL13-MC scanning mastercore data below 73 cm and EL09\_2B data after the latter was realigned with EL13-MC mastercore in Analyseries using the correlation of % sulphur with % of TSN sulphur data using a  $\mu$ -XRF Cr-tube (before alignment  $r^2=0.23$ ; after  $r^2=0.80$ ), and correlation of % TOC and inc./coh. scatter ratio data (before alignment  $r^2=-0.24$ ; after  $r^2=0.71$ ). Post-bomb (>1950 CE) radiocarbon age data were calibrated in CALIBOMB using the SH13 (Zone 1-2) post bomb curve and are shown in the table as pMC (percent modern carbon data). Calibrated ages have been rounded to the nearest five years where radiocarbon age errors are <50 years and 10 years where >50 years. The start of the rabbit influenced zone was Pb-210 dated to 1903±10 CE by Saunders et al.<sup>5</sup> and used as a correlation age constraint in the EL13 scanning mastercore.

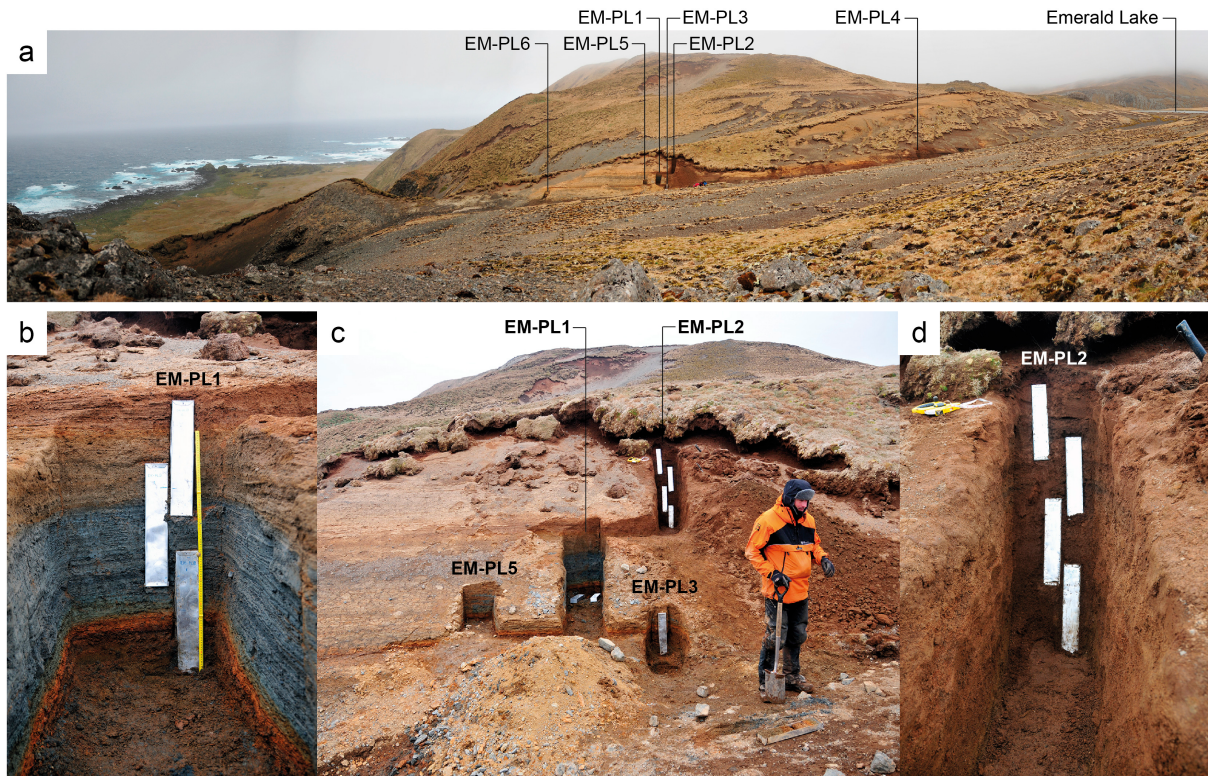
**Supplementary Table 2. Pb-210 ages from the uppermost 20 cm of the EL06 core used in the conductivity record in this study.**

EL06 Core Depth (cm)	Age (cal. a BP)		Mass Accumulation Rate ( $\text{g cm}^{-2} \text{a}^{-1}$ )	Year CE	
	CIC age $\pm 1\sigma$	CRS age $\pm 1\sigma$		CIC	CRS
0.25	1.4 $\pm$ 0.1	1.5 $\pm$ 0.4	0.127 $\pm$ 0.04	2005	2005
2.25	13.5 $\pm$ 1.0	14.5 $\pm$ 0.8	0.129 $\pm$ 0.007	1993	1992
4.25	24.7 $\pm$ 1.8	25.3 $\pm$ 0.9	0.136 $\pm$ 0.005	1981	1981
6.25	36.1 $\pm$ 2.6	35.4 $\pm$ 0.9	0.142 $\pm$ 0.004	1970	1971
8.25	48.1 $\pm$ 3.5	46.8 $\pm$ 0.9	0.143 $\pm$ 0.003	1958	1959
10.25	56.9 $\pm$ 4.1	57.7 $\pm$ 0.9	0.137 $\pm$ 0.002	1949	1948
12.25	64.4 $\pm$ 4.7	68.9 $\pm$ 0.9	0.13 $\pm$ 0.002	1942	1937
14.25	74.0 $\pm$ 5.4	82.2 $\pm$ 1	0.125 $\pm$ 0.001	1932	1924
16.25	83.7 $\pm$ 6.1	92.9 $\pm$ 1.1	0.125 $\pm$ 0.001	1922	1913
18.25	93.0 $\pm$ 6.8	104.8 $\pm$ 1.2	0.123 $\pm$ 0.001	1913	1901
20.25	102.7	Extrapolated max age of rabbit zone		1903	

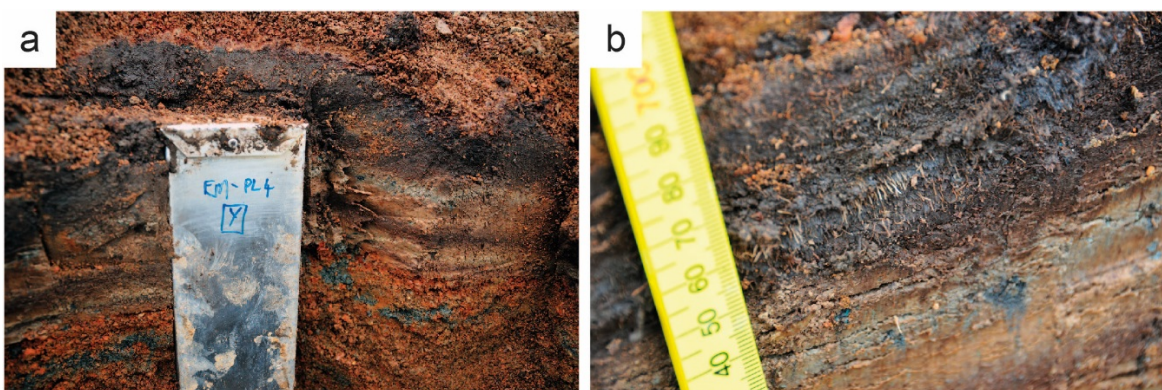
Notes: CIC = Constant Initial Concentration. CRS=Constant Rate of Supply. Full details of methods, data and CIC/CRS sedimentation models can be found in Saunders et al.<sup>5</sup>.

The weighted mean basal age of the conductivity and scanning records at 111 cm was 12,130 cal. a BP [12,060–12,220 min.–max. 95% confidence age range based on 2.5% and 97.5% quantiles from Bayesian age-depth modelling]. Whole record mean 95% age range uncertainties, rounded to the nearest 10 years are as follows. Conductivity record: 410 years [min. 4 years at 0–1 cm; max. 1,680 years at 21 cm]; scanning record: 410 years [min: 6 years at 0–1 cm; 4,240 years at 19 cm] (Supplementary Fig. 6; Supplementary Table 1).

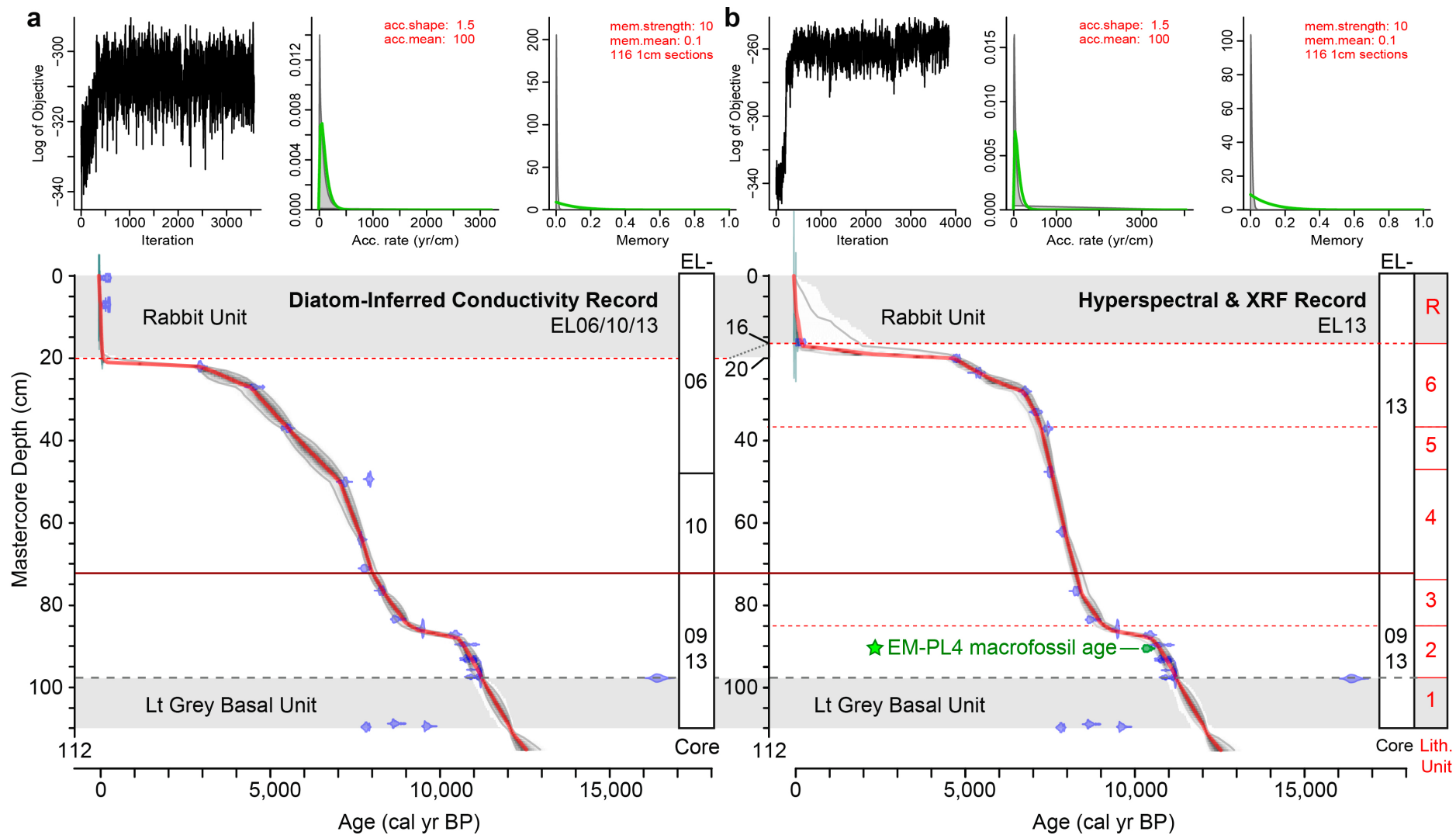
To test that the sequence is repeated in other lakes and to further constrain the age of the transition from the basal lithological unit, we dated a macrofossil-rich deposit immediately overlying equivalent basal green-grey sediments from a palaeolake immediately to the west of Emerald Lake. This is one of several lake sediment sections found on the west coast slope of Macquarie Island where cliff erosion has resulted in the drainage of cliff-top lakes and exposure of old lake sediments. Palaeolake sections (EM-PL: 1-6) were cut into a gully trending upwards towards Emerald Lake at c. NW-SE 60-240° relative to true N (Supplementary Figs. 4, 5). In EM-PL4, organic macrofossil-rich layers preserved in sequence are above the level of the green-grey basal clay-rich sediments, which are equivalent to the basal unit of EM-PL2. Sub-samples of the macrofossil-rich units were taken in the field for radiocarbon dating (Supplementary Table 1).



**Supplementary Figure 4. Emerald Palaeolake sediment sampling.** **a.** Cross section, approximately south-west (coast) to north-east (Emerald Lake), looking approximately north at palaeolake deposits in the gully below Emerald Lake. The locations of the sedimentary sections logged are shown, with the higher elevation of Emerald Lake apparent. All sections dip 15-20° to 240° (south-west) and into the cliff-face at 2-4° which required significant cutting back of c. 1-2 m to reach the true stratigraphy unaffected by slope deposition. **b.** Monolith tin samples taken from section of EM-PL1 showing the transitions from orange sandy-silt to green-grey clay/silt units near the base of the section. The green grey basal units have the same sedimentological characteristics as the basal unit of core EM-LIV1C. **c.** Close-up of the profiles dug in the central area. **d.** Sampling of section EM-PL2.



**Supplementary Figure 5** Sampling and close-up of the organic-rich unit in Emerald palaeolake section EM-PL4, located further upslope towards Emerald Lake. Macrofossils from this layer returned a date of  $9,230 \pm 40$   $^{14}\text{C}$  years BP, placing an absolute upper mean calibrated age limit of  $10,350 \pm 70$  cal. **a.** BP on the transition from the basal green-grey lithological clay-rich unit to more terrestrial conditions represented by Lithological Unit 2 in the Emerald Lake record.



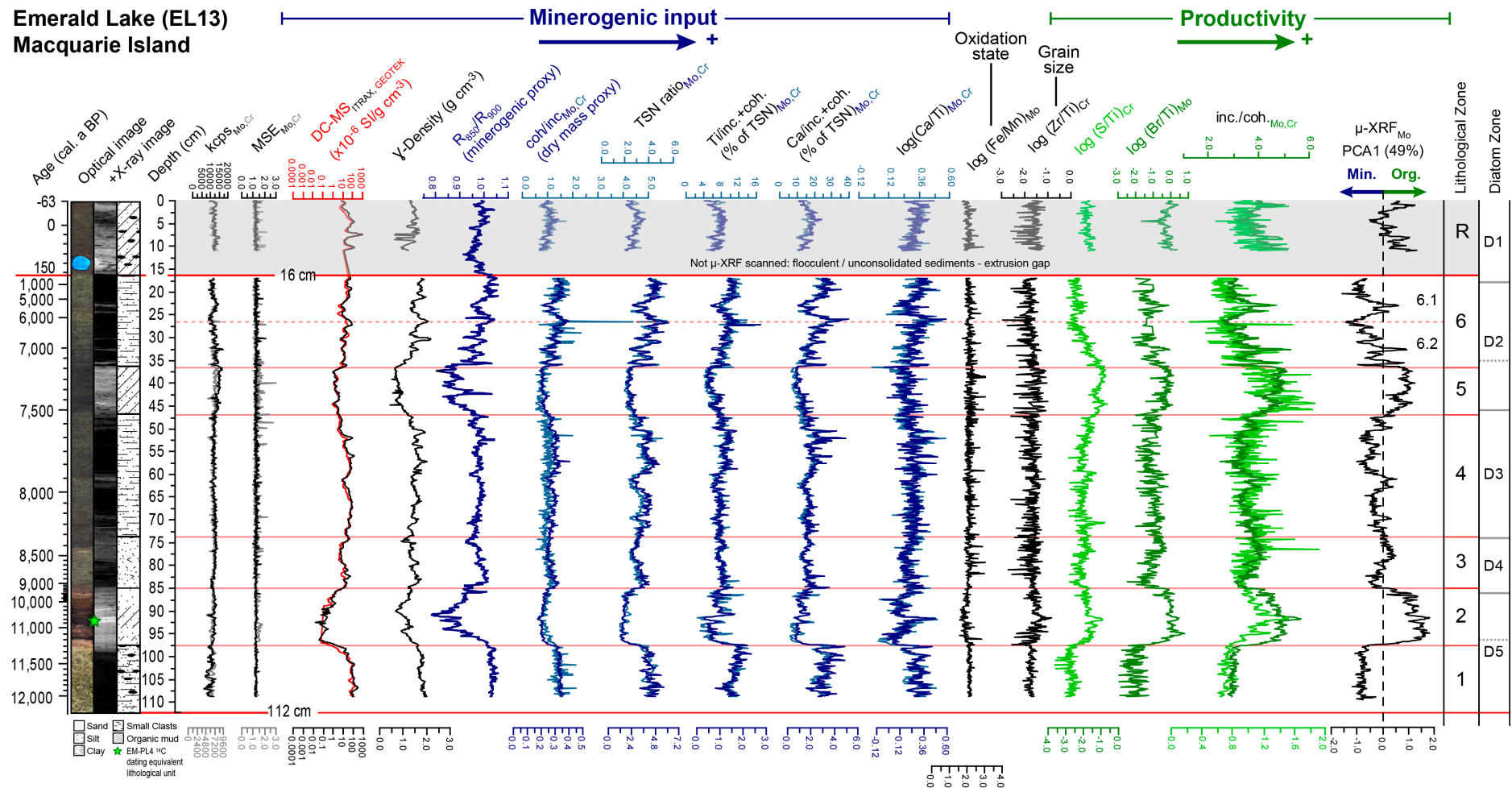
**Supplementary Figure 6. Age-depth models constructed for the conductivity and scanning records from Emerald Lake.** Sediment cores shown were collected between 2006–2013 (EL06, 09, 10, 13).

#### **Supplementary Note 4: Emerald Lake sedimentology, geochemistry and diatom analysis**

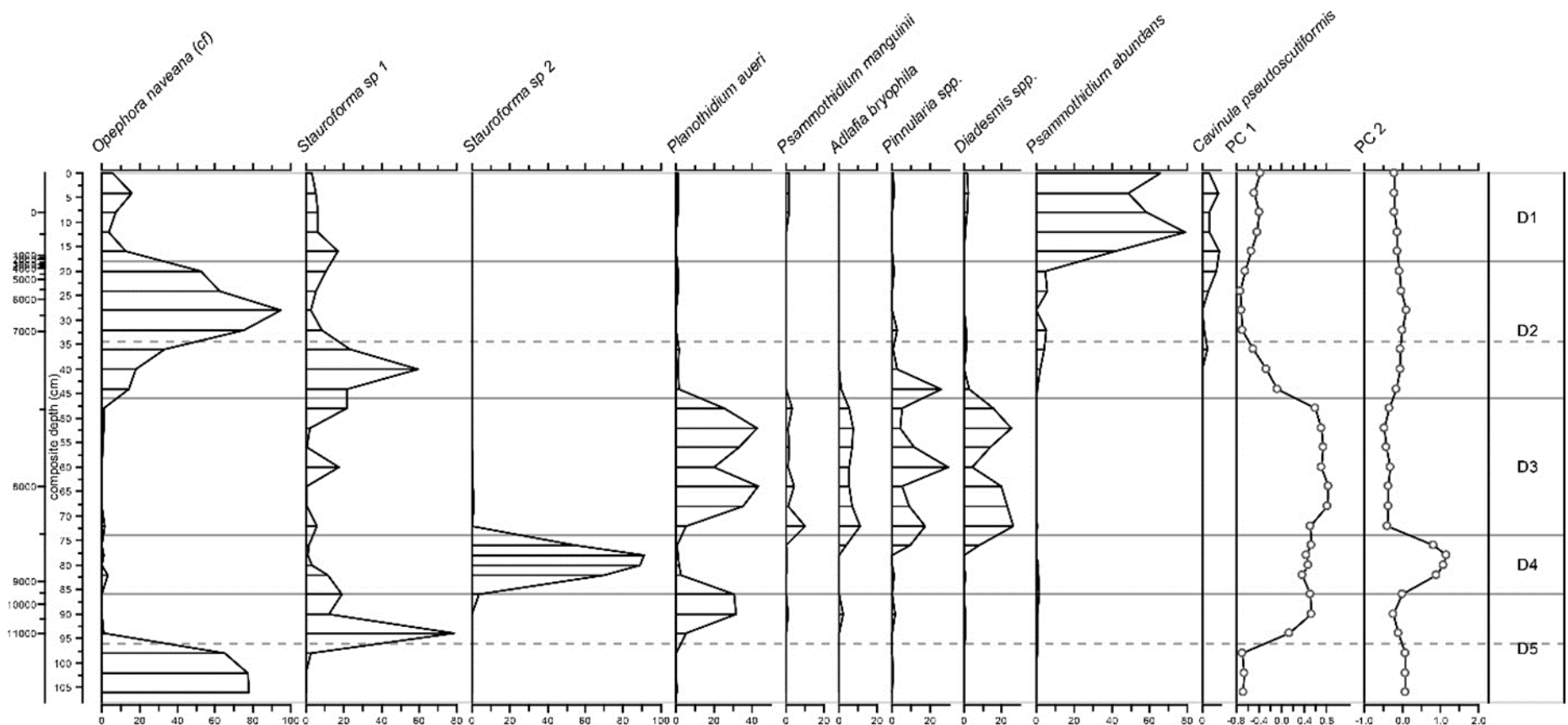
Sedimentological and geochemical data are shown in Supplementary Figure 7 and summarised and interpreted in Supplementary Table 3.

Lithological Units (1-6), and Diatom Zones (D1-5) were defined by constrained incremental sum of squares (CONISS) stratigraphically constrained cluster analysis with broken stick analysis in R packages vegan and rioja<sup>14</sup> (Supplementary Fig. 7). Hierarchical R-mode cluster analyses<sup>15</sup> were conducted on geochemical data with the R package 'Pvclust' (v. 1.2-236) using average linkage and a correlation-based dissimilarity matrix. Based on multi-scale bootstrap resampling ( $n=10,000$ ) approximately unbiased p-values were further calculated to assess the uncertainties in cluster analysis. R=Rabbit-influenced zone; Cr=Cr-tube  $\mu$ -XRF data; Mo=Mo-tube  $\mu$ -XRF data;  $\gamma$ -density=GEOTEK gamma-ray density; DC-MS=gamma density-corrected magnetic susceptibility; cps=count per second; MSE=Mean Square Error, low values <2 indicate a good fit to theoretical spectra (MSE mean $\pm 1\sigma$  values,  $n=1121$ : Mo-tube= $1.26\pm 0.11$ ; Cr-tube= $1.29\pm 0.20$ ; inc.=incoherent (inelastic, Compton) scatter; coh.=coherent (elastic, Rayleigh) scatter; inc.+coh.=total scatter; TSN=Total Scatter Normalised ratio, which was calculated as the sum of an individual element/(inc+coh), inc.//(inc.+coh.) and coh.//(inc.+coh.) cps ratios. Since this simplifies to Total element/(inc.+coh.) +1, the influence of scatter in wet sediment scanning is reduced to a constant value, enabling more effective comparison with dry and organic-free sediment sub-samples used in traditional XRF analysis<sup>16-19</sup>. Higher TSN values indicate increased sediment mineral (or tephra) content and, along with coh/inc ratios, broadly correspond to changes in dry mass accumulation<sup>19,20</sup>. Key element/Ti log-ratios (Ca/Ti, Br/Ti) used here have been shown to compare favourably with Al- and Ti-normalised patterns in sub-sample  $\mu$ -XRF data in previous studies (e.g., ref. 16, 19). Measurement and running mean errors are not shown for clarity, but are typically <10%. The first Principal Components Analysis axis explains 49% of the variance in  $\mu$ -XRF Mo-tube dataset, with negative values reflecting increased minerogenic inputs and positive values increased organic productivity.

The past diatom composition of the lake also provides information on changes in the lake ecology (Supplementary Fig. 8; Supplementary Table 3). Earliest high conductivity periods are marked by the predominance of salt-tolerant species *Opephora naveana* (cf.). The reduction in conductivity is evident with a shift away from *Opephora naveana* (cf.) and its replacement by a benthic community consisting of sub-Antarctic varieties of *Stauroforma*, and by a brief period dominated by moss-and soil-associated taxa (8.2–7.4 cal ka BP) which suggest reduced precipitation and lake level lowering. This lake level lowering may partly explain the brief negative correlation between the minerogenic proxies and diatom-inferred conductivity between 7.5–7.2 cal ka BP. After 7.4 cal ka BP, *Opephora naveana* (cf.) reappears as the most common diatom and suggests higher lake levels and higher conductivity at Emerald Lake. Over the late mid- to late-Holocene, it is progressively replaced by freshwater taxa (e.g. *Psammothidium abundans*, *Cavinula pseudoscutiformis*) until the present day.



**Supplementary Figure 7. Summary sedimentology, μ-XRF core scanning geochemical data and interpretation of the EL13 Emerald Lake composite record.** These data show that μ-XRF Ti is representative of increased minerogenic input into Emerald Lake. Full caption on previous page.



**Supplementary Figure 8. Emerald Lake diatom species diagram from the EL13 cores.** This summary diagram shows the relative frequency of key taxa, Principal Component Analysis (PC) axes 1 and 2, and significant floristic zones D1-D5, which were used in combination with the sedimentological data shown in Supplementary Figure 7 to establish the palaeoenvironmental interpretation for Emerald Lake shown in Supplementary Table 3.

**Supplementary Table 3. Summary sedimentology, diatom flora and interpretation.**

Lith. Unit	Depth (cm)	Modelled Age (cal. a BP)		Munsell Colour	Summary sedimentology	Diatom Zone	Dominant Diatom Flora	Summary Palaeoenvironmental Interpretation	Southern Westerly Wind strength
		Weighted mean	95% min — 95% max						
R	0 — 16	<b>-63 — 170</b>	-67 — 1830	10YR 3/2 & 3/4	Flocculent brown-grey organic-rich mud with some sand; 0-2 cm contains living green algae	D1	<i>Psammothidium abundans</i> , <i>Cavinula pseudoscutiformis</i>	Rabbit-influenced with significantly increased catchment erosion rate	Dips below mean then increases
6	16 — 36.3	<b>170 — 7,210</b>	25 — 7,360	10YR 4/1 & 3/3	Brown-grey banded muddy sand grading upwards into a consolidated fine-medium grained dark grey-green sandy silt with occasional moss and macrofossil fragments	D2.2	<i>Opephora naveana</i> (cf.)	Initially increasing aeolian deposition, with elevated salinity and aerosol deposition, followed by reduced reconstructed conductivity from 6000-5000 cal. a BP, increasing to 4000 and stabilising from 4000 cal. a BP onwards	Consistently above mean
5	36.3 — 46.6	<b>7,210 — 7,520</b>	7,030 — 7,610	10YR 2/2 & 4/1	Brownish-grey sandy silt with some coarse sand and sharp lower boundary fining upwards into a dark brown organic-rich mud with some silt	D2.1	<i>Stauraformosa species 1</i>		
4	46.6 — 73.5	<b>7,520 — 8,320</b>	7,400 — 8,510	10YR 3/2 & 2.5Y 4/2	Banded grey clayey sand and brown organic rich muddy sand	D3	<i>Planothidium aueri</i> , <i>P. mangunii</i> , <i>Adlaafia bryophila</i> , <i>Pinnularia spp.</i> , <i>Diadesmis spp.</i>	Moss- & soil- associated sedimentology and diatom taxa, associated with reduced precipitation, lower lake levels and aerosol inputs	At, or above mean
3	73.5 — 84.9	<b>8,320 — 9,150</b>	8,180 — 9,410	10YR 3/2 & 2.5Y 4/2	Grey-green clay/sand grading upwards into a brown-grey muddy sand capped by light greyish brown silty-clay	D4	<i>Stauraformosa species 2</i>	Initially elevated meltwater-related catchment inputs followed declining mineralogenic inputs and unclear ecological affiliations. Higher, but fluctuating reconstructed conductivity suggests strengthened SHW strength	Greater than 95% upper bound mean
2	84.9 — 97.5	<b>9,150 — 11,230</b>	8,940 — 11,300	2.5Y 3/3 & 2.5/1	Very dark brown (well-humified) mud grading upwards into a banded dark brown capped by dark orange organic rich muddy sand	D5.2	<i>Stauraformosa species 1</i>	Initially terrestrial conditions with reduced precipitation, lower lake levels	Consistently below mean
1	97.5 — 112	<b>11,230 — 12,240</b>	11,100 — 12,460	5G 4/1	Light greenish-grey medium-coarse grained silty-clay with some sand and c. 1 mm black clasts. Similar to the distinctive basal units of palaeolake cliff sequence adjacent to Emerald Lake	D5.1	<i>Opephora naveana</i> (cf.)	Devegetated catchment with increased precipitation causing elevated meltwater input combined with high salinity and aerosol input associated with increased Westerly Wind strength	Greater than 95% upper bound mean

Notes: Based on the descriptions and diatom analysis of the scanning mastercore.

## **Supplementary Note 5: Wind proxies**

A combination of three methods was used to reconstruct past changes in SHW intensity. Diatom-based inference models provided a measure of past sea salt aerosol inputs and were compared with two independent measures of minerogenic aerosol inputs. The statistically significant correlations between the three proxies (Supplementary Table 4) suggests that changes in the proxies are primarily a result of changes in aerosol delivery by the SHW rather than local catchment processes such as vegetation change or erosion.

Down core trends in diatom and geochemical datasets using Principal Components Analysis (PCA) were summarised using C2 software<sup>21</sup> and square-root normalised standardised (mean- $1\sigma$ )  $\mu$ -XRF (Total Scatter Normalised (TSN)) percentage geochemical data (which is not directly equivalent to whole rock percentage data), and percentage diatom count data. Additional statistical analysis and plotting of data were undertaken in C2 v.1.7.612439, XLStat v.2010.3.09, SigmaPlot v.13, and AnalySeries v.2.0.4 software<sup>22</sup>. Downcore cluster-zonation was undertaken on ecologically-grouped diatom percentage data and square-root transformed and standardised (mean- $1\sigma$ ) geochemical data in RStudio v. 0.98.939 using the R v.3.0.1 and Community Ecology Packages Vegan v.2.0-10 37 and Rioja v.0.8-5<sup>23</sup>.

### *Diatom-based inference models*

The ion chemistry of Macquarie Island lakes is dominated by the input of sea salt aerosols. This is reflected in the similarity of the ionic and cationic proportions in the lakes to that of seawater: Na > Mg > Ca > K > Cl > SO<sub>4</sub> > HCO<sub>3</sub>. The aerosol inputs are the result of the transfer of sea salt particles via sea spray, and sea salts scavenged from the air as moisture and salt-laden air masses rise over the island and cool; the latter being the dominant source of precipitation. Studies on other sub-Antarctic islands have shown that the concentration of the sea salts (based on a positive matrix factorisation analysis of the various source contributions to the submicron aerosol organic matter in sea spray) is dependent on wind speed<sup>24</sup>. In their experiment, concentrations increased slightly between 8 and 10 ms<sup>-1</sup>, and by approximately a factor of three at wind speeds greater than 10 ms<sup>-1</sup><sup>24</sup>. The volume of sea salt aerosols delivered to the lakes is therefore a function of the strength of the westerly winds and distance from the ocean<sup>6,25</sup>. As a result, the lakes on Macquarie Island show statistically significant ( $p<0.005$ ) west to east gradients in conductivity. Changes in the balance between zonal precipitation and wind driven evaporation could also have an impact on the salinity of the lakes but is likely to be of secondary importance as meteorological measurements have shown that sea spray precipitation deposits between 2433 and 220 kg ha<sup>-1</sup> yr<sup>-1</sup> NaCl at different sites on the island<sup>26</sup>. This is supported by this study, which show that periods of higher rainfall (lake levels inferred from diatom species composition) correspond with periods of elevated D-I conductivity (Supplementary Table 3).

Salinity (measured here as conductivity) also influences the composition of biological communities in the lakes. Diatom species assemblages are primarily structured by salinity, although nutrients, temperature and pH also explain an independent portion of the variance<sup>27</sup>. The diatom-conductivity transfer function utilises the strong statistical relationship between modern diatom species assemblages and lake water conductivity (weighted averaging partial least squares, two components;  $r^2 = 0.92$ ,  $r^2_{jack} = 0.72$ , RMSEP=230  $\mu$ S cm<sup>-1</sup>) to reconstruct past changes in conductivity from subfossil species assemblages preserved in the lake sediments<sup>27,28</sup>. The Saunders et al. diatom transfer function was modified to reconstruct conductivity (the published version is based on salinity) and adjusted to take account of recent changes in diatom taxonomy. Both the Saunders et al<sup>27</sup> and Van Nieuwenhuyze et al.<sup>28</sup> transfer functions gave similar results. The resolution of the diatom-inferred conductivity reconstruction was 5 mm, equivalent to, on average, 55 years.

### *Micro-XRF Core scanning*

Our second method of inferring past SHW at Macquarie Island was to track the input of potential ‘sea-spray’ derived aerosols (e.g., Mg, Na, Cl, Br)<sup>16</sup>, wind-blown minerogenic (dust) aerosols (e.g., elevated Titanium, Ti, and other ‘crustal’ elements such as Al, K, Sr)<sup>29</sup>, and minerogenic sediment in-washed from the catchment into the lake (e.g., Ti<sup>30</sup>). Many elements found in sea-spray (e.g., K, Ca, Sr) are found in greater concentrations in lake sediment and catchment soil. We focused on ‘wind-blown’ and in-washed minerogenic elements that are routinely well-measured using the ITRAX  $\mu$ -XRF core scanner, principally titanium (Ti). Titanium is the least post-depositionally altered of several ‘crustal’ elements found in wind-blown material, and not influenced by biological transformation associated with within-lake processes (Supplementary Figs. 7, 9).

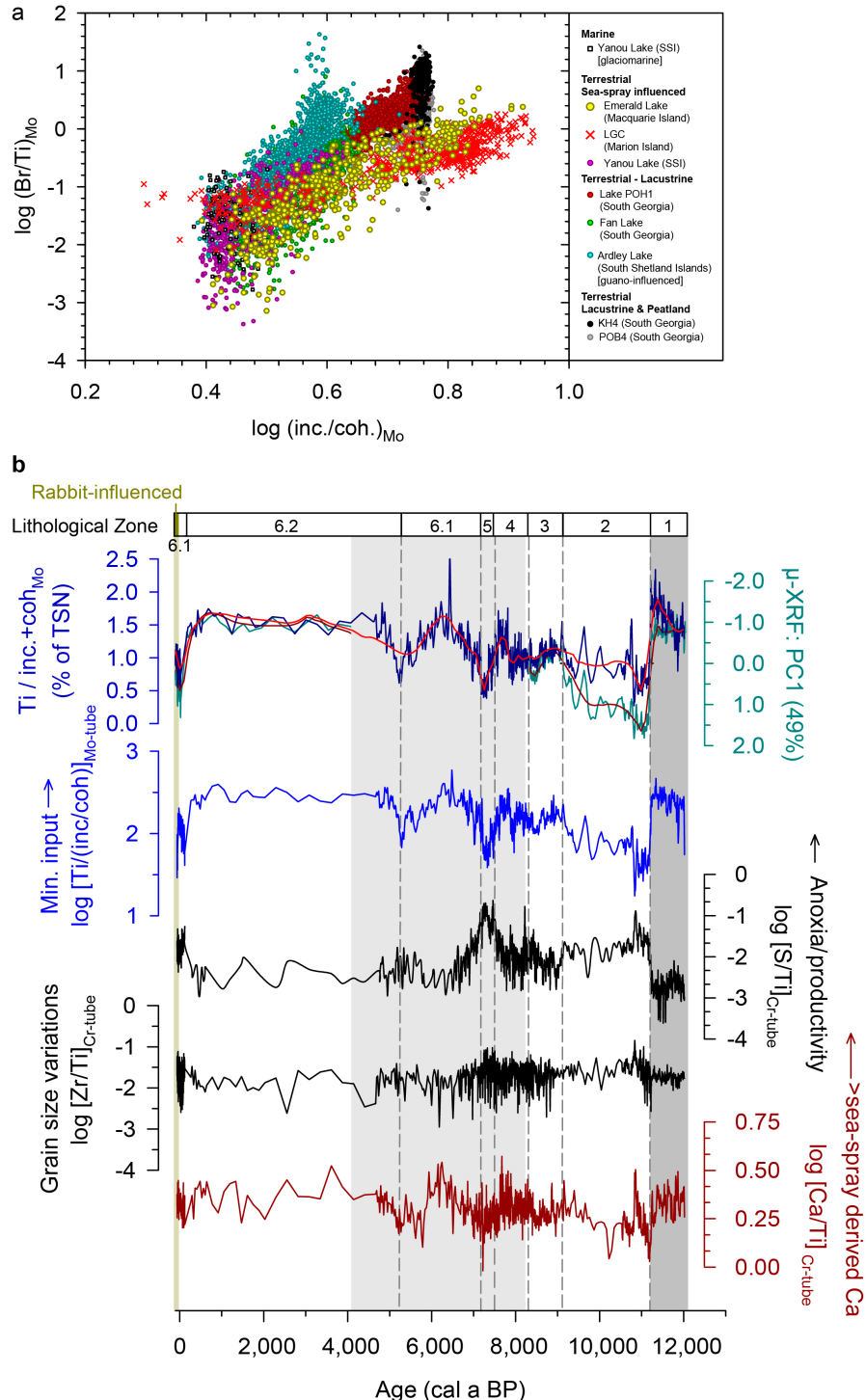
Replicate multiple element scans were undertaken using Molybdenum (Mo) then Chromium (Cr) X-ray tubes (settings Mo tube: 30 kV, 50 mA, 10 second measurement interval; Cr-tube: 30 kV, 40 mA, 10 seconds). Micro-XRF scanning was undertaken at 200  $\mu$ m or 1 mm intervals and data are presented as 1 mm intervals (based on five-point running mean where appropriate), equivalent, on average, to c. 11 years. Machine and sample calibration was undertaken using synthetic glass standards and XRF fused glass discs from Antarctic lake cores at the start, middle and end of each session. X-radiographic scans were undertaken prior to  $\mu$ -XRF analysis at 60  $\mu$ m intervals (settings: 45 kV, 50 mA, 200 ms). XRF spectra peak areas were quantified using Q-Spec 6.5 software and element and scatter parameter counts per second (cps) were normalised by the total scatter cps (incoherence + coherence, inc.+coh.) to account for downcore variations in water content and organic matter. Data are presented as percentages of the total scatter-normalised ratio (TSN) to examine covariance between measured elemental and scattering parameters (after<sup>19</sup>). This method also avoids creating spurious patterns for elements that cannot be easily measured (e.g., Na, Mg) or commonly return low cps values (e.g., Al) with ITRAX analysis<sup>16-18,31</sup>.

Whole core gamma (bulk) density (2 mm aperture gamma ray attenuation sensor), magnetic susceptibility (MS) (Bartington Instruments MS2C loop sensor, 10 second measurement time), resistivity and P-wave velocity were measured with a GEOTEK core logger and standard calibration procedures (Gunn and Best, 1998). Magnetic susceptibility was also measured immediately after  $\mu$ -XRF scanning using an MS2E point sensor at 2 mm intervals and measurement time of 10 seconds (Supplementary Figure 7).

Of the potential sea-spray derived aerosols, only Br and Ca have sufficient  $\mu$ -XRF count rates to be useful. Comparison of  $\mu$ -XRF data from Emerald Lake with other lake sediment and peatland data from the (sub)-Antarctic shows that Br deposition in Emerald Lake is likely related to changes in the incoherent/coherent (inc./coh.) scatter ratio, commonly used as a proxy for changes in organic and water content<sup>16,32</sup> (Supplementary Fig. 9a). Since there is no major variation in grain-size or significant relationship between Ca and organic or sulphur content, elevated excess Ca, shown by log[Ca/Ti] in Supplementary Fig. 9b, broadly corresponds to downcore Ti variation, and, therefore, most likely reflects phases of increased deposition of sea-spray aerosol Ca (Supplementary Fig. 9b).

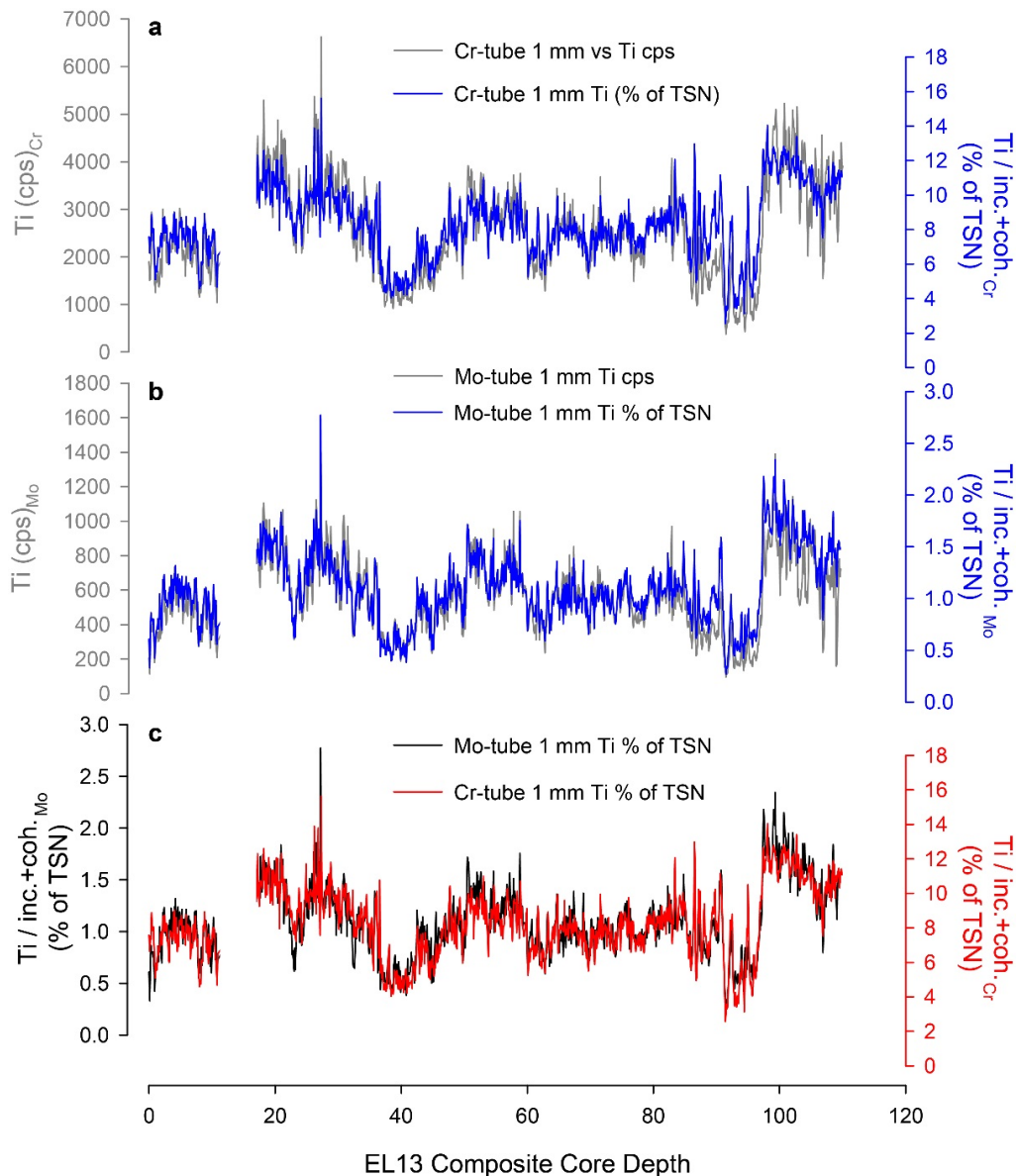
The micro-XRF PCA Axis 1 plot in Fig 2 (main text) explains 49% of the variance in the micro-XRF dataset for elements and scattering parameters that consistently make up >95% of the measured counts per second. Negative values reflect elements and scattering parameters or ratios commonly associated with increased minerogenic input (e.g., coh. /inc. ratio, Ti, Ca, K, Rb, Sr, Fe, Zn, where elevated coh. /inc. ratio values reflect increased dry mass), while positive PCA1 values reflect increased organic productivity within the lake (e.g., inc., coh., inc./coh. and Br). We use  $\mu$ -XRF Ti data and the Hyperspectral index  $R_{850}/R_{900}$

optical ratio to track minerogenic aerosol and other minerogenic inputs into Emerald Lake. The significant 100-year interval correlations between these parameters, the micro-XRF PCA Axis 1 data and increased conductivity (Supplementary Tables 4) means that both Ti and  $R_{850}/R_{900}$  can also be used as high-resolution proxies for changes in the relative strength of the SHW at this location.



**Supplementary Figure 9.** Potential sea-spray indicators from  $\mu$ -XRF scanning data **a**. Bi-plot of  $\log (\text{Br}/\text{Ti})$  and  $\log (\text{inc.}/\text{coh.})$  scattering data (all Mo-tube) from  $\mu$ -XRF scans of lacustrine and peatland records on South Georgia, South Shetland Islands compared with data collected from sea-spray influenced lake records on Macquarie Island (Emerald Lake)

and other sub-Antarctic islands. All data were analysed and processed data in the same manner. **b.** Comparison between the  $\mu$ -XRF Titanium wind-proxy and commonly used  $\mu$ -XRF proxies for lake anoxia ( $\log[S/Ti]$ ), grain-size ( $\log[Zr/Ti]$ ) and sea-spray aerosol derived Calcium ( $\log[Ca/Ti]$ ) in the Emerald Lake sediment record.



**Supplementary Figure 10.** Consistency and reproducibility of scanning Ti data. **a.** Comparison between Ti cps and Ti/inc.+coh. ratios (expressed as a percentage of the Total Scatter Normalised, TSN, ratio defined in Supplementary Figure 7), measured using an ITRAX  $\mu$ -XRF scanner fitted with a Cr-tube. **b.** Comparison between Ti cps and Ti/inc.+coh. ratios (expressed as a percentage of the TSN ratio defined in Supplementary Figure 7), measured using an ITRAX  $\mu$ -XRF scanner fitted with a Mo-tube. **c.** Comparison of Ti/inc.+coh. ratio data measured with Cr- and Mo-tubes. See text for run settings. Note the excellent reproducibility and coherence between datasets shown.

### *Hyperspectral core scanning*

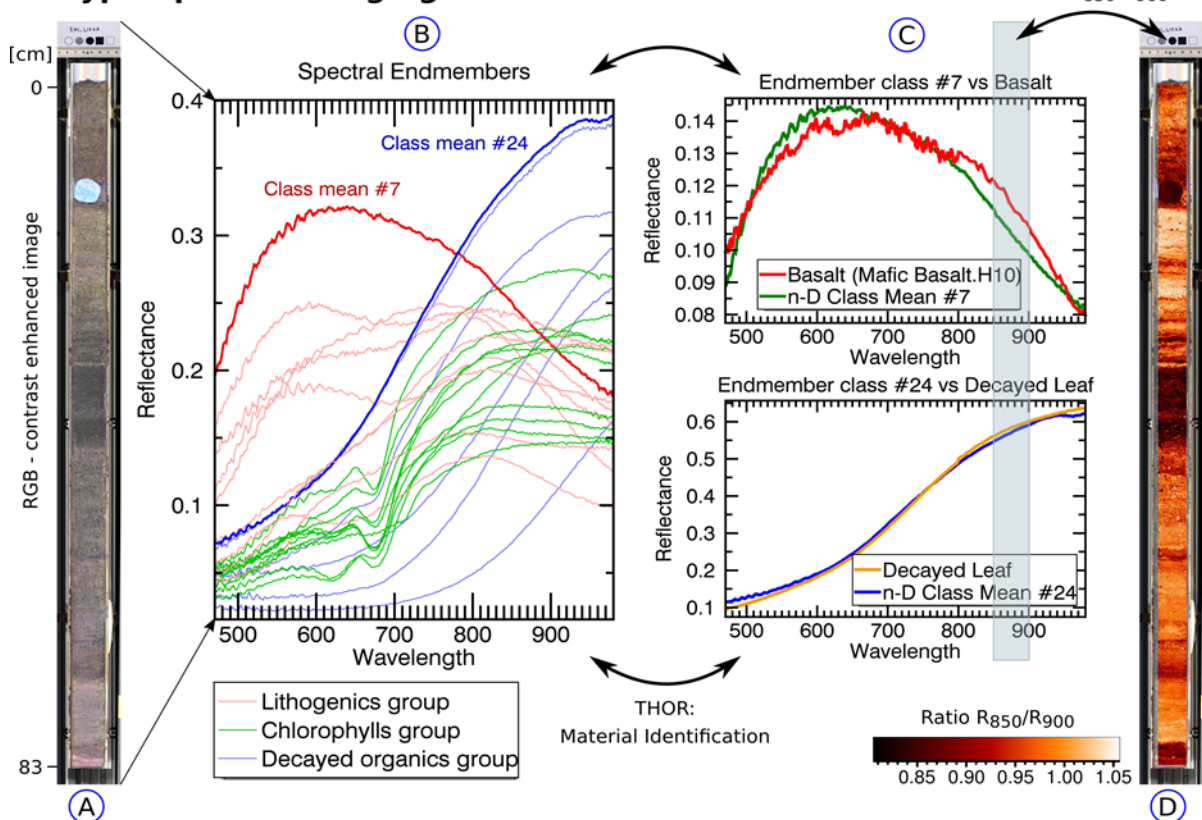
Our third method of inferring past SHW was also based on detecting mineralogenic aerosol and other mineralogenic inputs into the lake sediments using optical methods. Cores were scanned using a Specim hyperspectral imaging core scanner. The Specim Ltd. scanner consists of a hyperspectral camera and a sample tray that moves underneath an illumination chamber and the camera slit. The camera takes reflectance spectra from the sediment surface in the visible to near infrared spectrum from 400–1000 nm with a spectral resolution of 2.7 nm, sampled at 0.8 nm with a radiometric resolution of 12 Bit 26. The spatial resolution (pixel size) can be as small as 38 x 38  $\mu\text{m}/\text{pixel}$ . Data normalisation and analysis were made using ENVI 5.0 sp3 (EXELISVIS ENVI, Boulder, Colorado) remote sensing software<sup>33</sup>. The spatial resolution of the hyperspectral scans was set to 69 microns which is theoretically equivalent to 0.75 years in the Emerald Lake EL13 record.

Previous studies have shown that spectral indices, characteristic of lithogenic materials such as the Ratio  $R_{570}/R_{630}$ , compare very well with analytical measurements (typical  $R^2$  between 0.70 and 0.98)<sup>27</sup>. The index  $R_{570}/R_{630}$  is based on the spectral properties of the clay minerals Illite and chlorite which peak at  $R_{570}$  and show a descending trend thereafter. Organic compounds, however, usually show an increasing trend in the region of  $R_{570}$  and  $R_{630}$ . Thus, the index  $R_{570}/R_{630}$  explains the ratio between specific clay minerals and organic compounds in the sediment core<sup>34</sup>.

For Emerald Lake, the geological background is based on basaltic rocks (Geology map: [http://www.mrt.tas.gov.au/mrtdoc/map\\_catalogue/map\\_public/898413\\_1/macq50cat.pdf](http://www.mrt.tas.gov.au/mrtdoc/map_catalogue/map_public/898413_1/macq50cat.pdf)).

This requires a spectral index adapted to basaltic host rock instead of the spectral index  $R_{570}/R_{630}$ . Supplementary Figure 11 shows the method development of such an index. Supplementary Figure 11a shows a red–green–blue (RGB) band combination of the hyperspectral image of the sediment core and Figure 11b the spectral endmembers derived from the sediments using ENVI's Spectral hourglass procedure. Spectral endmembers are a representative sample of all sediment-spectra in the image depicting the purest materials. Comparison of endmember spectra to mineral standards from a spectral library allow identification of sediment components. In Supplementary Figure 11c two endmember spectra have been identified as mafic basalt and decayed leaf using the THOR material identification tool from the ENVI software. The mafic basalt shows a strong decreasing trend in the region between  $R_{850}$ - $R_{900}$  whereas the decayed leaf shows a strong increasing trend in the same region. Based on this information, the other endmembers can be divided into three groups: One group associated with lithogenic materials showing a strong decreasing trend in  $R_{850}$ - $R_{900}$ , one group associated to decayed organic compounds showing a strong increasing trend, and one group that shows a flat trend at  $R_{850}$ - $R_{900}$ . The last group also shows an absorption band at  $R_{673}$ , which is most likely caused by chlorophyll pigments. Supplementary Figure 11d shows the result of the ratio  $R_{850}/R_{900}$  as a colour-mapped image where black to red colours depict a decreasing trend, and orange to white colours an increasing trend.

## Hyperspectral imaging and material identification



**Supplementary Figure 11.** SPECIM hyperspectral core scanning method development showing. **a.** Contrast-enhanced RGB band combination of the core. **b.** Spectral endmembers derived from the data using the Spectral hourglass procedure of the ENVI Software. **c.** Scaled comparison of selected endmembers with available spectral libraries using ENVI's THOR Material identification tool. **d.** Colour mapped image of the Ratio at the reflectance  $R_{850}/R_{900}$ .

### Correlations between wind proxies

We investigated the relationships between the three new wind proxies from Emerald Lake, and between the new wind proxies from Emerald Lake and atmospheric CO<sub>2</sub>, temperature and sea ice (based on proxies in the EPICA Dome C ice core), and marine core microfossil-based measurements of winter sea-ice extent (WSI%) in selected (and not necessarily representative) marine cores from the South Atlantic (PS2090<sup>35</sup>) and South Pacific sector near Macquarie Island (E27-23<sup>36</sup>) (see Supplementary Note 8 for data sources). Our detailed age depth modelling (Supplementary Note 3) was essential to this analysis as age uncertainty is the largest contributor to estimation error for time series similarity<sup>37</sup>.

First, we undertook normality tests and simple correlation analysis of the data and residuals using the 2<sup>nd</sup> order polynomial LOESS (Local tricube weighting and polynomial regression) smoothed 100-year interval datasets (red lines in Figures 2 and 3). It is important to note that the as-measured conductivity dataset was the only dataset that was normally distributed and that this analysis does not include a correction for serial temporal autocorrelation or take account of underlying cyclicity present in the datasets (Supplementary Tables 4,5,7). As a first order experiment, we examined two scenarios, first excluding the top of the core (from 1500 yr BP to present), which was too flocculent for the core scanning methods, and, second, excluding the lower resolution part of the core to test relationships in the 4,000–12,000 yr BP period only (not shown). The obvious reduction in the correlation coefficients

and p-value significance levels between the LOESS 100-yr smoothed data and their respective residuals indicates that, as expected, serial autocorrelation or underlying cyclicity is a significant issue for all datasets (including the ice and marine core data, Table 5), requiring more complex statistical analysis.

**Supplementary Table 4. Simple Pearson Correlation Coefficients and *p*-values for wind proxy data from Emerald Lake compared with published 1,500–12,000 yr BP LOESS 100-year smoothed datasets.**

Summary statistics: Data (100-yr 2nd order poly LOESS smoothed; n=106; 1.5-12 ka)

Variable	Minimum	Maximum	Mean	Std. dev.
D-I Cond.	64.71	524.13	302.99	113.01
Ti <sub>Mo</sub> (%TSN)	0.51	1.89	1.25	0.30
inc/coh <sub>Mo</sub>	2.75	5.04	3.51	0.63
PCA1 <sub>Mo</sub>	-1.12	1.64	-0.27	0.74
R <sub>850/R<sub>900</sub></sub>	0.86	1.06	0.98	0.05
WSI-a %	-4.42	41.44	26.45	15.15
WSI-b %	-2.47	48.73	13.85	10.52
EDC-Na	41.84	63.82	50.32	5.54
EDC-TA	-2.38	0.29	-0.49	0.48
EDC CO <sub>2</sub>	240.92	278.82	265.32	7.95

Correlation matrix (Pearson): Data (100-yr LOESS Interpolated)

Variables	D-I Cond.	Ti <sub>Mo</sub> (%TSN)	inc/coh <sub>Mo</sub>	PCA1 <sub>Mo</sub>	R <sub>850/R<sub>900</sub></sub>	WSI-a %	WSI-b %	EDC-Na	EDC-TA	EDC CO <sub>2</sub>
D-I Cond.	1	<b>0.649</b>	-0.699	-0.735	0.557	<b>0.668</b>	<b>0.231</b>	<b>0.350</b>	-0.003	<b>0.215</b>
Ti <sub>Mo</sub> (%TSN)		1	<b>-0.921</b>	-0.907	<b>0.846</b>	<b>0.430</b>	0.145	<b>0.359</b>	<b>0.281</b>	<b>0.262</b>
inc/coh <sub>Mo</sub>			1	<b>0.991</b>	-0.912	-0.597	-0.197	-0.477	-0.134	-0.226
PCA1 <sub>Mo</sub>				1	-0.900	-0.667	-0.213	-0.479	-0.124	-0.243
R <sub>850/R<sub>900</sub></sub>					1	<b>0.521</b>	0.057	<b>0.414</b>	0.178	0.162
WSI-a %						1	0.161	<b>0.384</b>	<b>0.223</b>	<b>0.484</b>
WSI-b %							1	<b>0.347</b>	-0.159	0.016
EDC-Na								1	-0.203	0.160
EDC-TA									1	<b>0.707</b>
EDC CO <sub>2</sub>										1

Values in bold are different from 0 with a significance level alpha=0.05; values shaded red(+) & blue(-) are significantly correlated (*p*<0.05)

p-values: Data (100-yr 2nd order poly LOESS smoothed)

Variables	D-I Cond.	Ti <sub>Mo</sub> (%TSN)	inc/coh <sub>Mo</sub>	PCA1 <sub>Mo</sub>	R <sub>850/R<sub>900</sub></sub>	WSI-a %	WSI-b %	EDC-Na	EDC-TA	EDC CO <sub>2</sub>
D-I Cond.	0	<b>&lt; 0.0001</b>	<b>&lt; 0.0001</b>	<b>&lt; 0.0001</b>	<b>&lt; 0.0001</b>	<b>&lt; 0.0001</b>	<b>0.017</b>	<b>0.0002</b>	0.977	<b>0.027</b>
Ti <sub>Mo</sub> (%TSN)	0	<b>&lt; 0.0001</b>	<b>&lt; 0.0001</b>	<b>&lt; 0.0001</b>	<b>&lt; 0.0001</b>	<b>&lt; 0.0001</b>	0.138	<b>0.0002</b>	<b>0.004</b>	<b>0.007</b>
inc/coh <sub>Mo</sub>		0	<b>&lt; 0.0001</b>		<b>&lt; 0.0001</b>	<b>&lt; 0.0001</b>	<b>0.043</b>	<b>&lt; 0.0001</b>	0.170	<b>0.020</b>
PCA1 <sub>Mo</sub>			0		<b>&lt; 0.0001</b>	<b>&lt; 0.0001</b>	<b>0.028</b>	<b>&lt; 0.0001</b>	0.206	<b>0.012</b>
R <sub>850/R<sub>900</sub></sub>				0	<b>&lt; 0.0001</b>	<b>0.560</b>	<b>&lt; 0.0001</b>	0.068	0.096	
WSI-a %					0	0.100	<b>&lt; 0.0001</b>	<b>0.022</b>	<b>&lt; 0.0001</b>	
WSI-b %						0	<b>0.0003</b>	0.104	0.873	
EDC-Na							0	<b>0.037</b>	0.100	
EDC-TA								0	<b>&lt; 0.0001</b>	
EDC CO <sub>2</sub>									0	

Values in bold are different from 0 with a significance level alpha=0.05; values shaded red(+) & blue(-) are significantly correlated (*p*<0.05)

Notes: This provides a first order assessment of the relationships between these datasets and is based on the LOESS 2<sup>nd</sup> order polynomial smoothed 100-year interval data, without correction for serial autocorrelation in individual time series; inc/coh<sub>Mo</sub> ( $\mu$ -XRF) has been used extensively as an organic proxy<sup>16</sup> and is included here as a control. As expected, it is strongly correlated with the  $\mu$ -XRF PCA1 data because the incoherent and coherent scatter constitute  $34.5 \pm 12.9\%$  (mean $\pm 1\sigma$ ) of the total scatter-normalised 1 mm dataset and  $\mu$ -XRF-PCA1 accounts for 49% of the variance in the data, as shown in Figure 2 and Supplementary Figure 7. R<sub>850/R<sub>900</sub></sub> (hyperspectral imaging) and Ti (% TSN<sub>Mo</sub>) ( $\mu$ -XRF) are proxies for mineralogenic input as defined in Supplementary Figure 7. D-I Cond refers to the Weighted Average Partial Least Squares Conductivity transfer function reconstruction shown in Figure 2. WSI is the winter sea ice proxy in PS2090, EDC-Na is EPICA Dome C Na-flux

data; EDC-TA is EPICA Dome C Temperature Anomaly data; EDC-CO<sub>2</sub> is EPICA Dome C CO<sub>2</sub> data.

**Supplementary Table 5. Pearson Correlation Coefficients and *p*-values for residuals from wind proxy data from Emerald Lake compared with key Southern Ocean and Antarctic data (1,500–12,000 yr BP LOESS 100-year smoothed datasets).**

Summary statistics: Residuals (100-yr LOESS Interpolated; n=106; 1.5-12 ka)

Variables	Minimum	Maximum	Mean	Std. dev.
D-I Cond.	-94.13	69.18	3.57	29.03
Ti <sub>Mo</sub> (%TSN)	-0.36	0.36	0.00	0.13
inc/coh <sub>Mo</sub>	-0.45	0.66	-0.01	0.17
PCA1 <sub>Mo</sub>	-0.46	0.59	0.01	0.18
R <sub>850</sub> /R <sub>900</sub>	-0.06	0.03	0.00	0.01
WSI-a %	-8.21	8.34	0.03	2.68
WSI-b %	-4.71	9.25	0.29	2.58
EDC-Na	-13.09	16.81	-0.03	3.96
EDC-TA	-0.71	0.77	-0.01	0.29
EDC CO <sub>2</sub>	-2.57	1.92	0.03	0.89

Correlation matrix (Pearson): Residuals (100-yr LOESS Interpolated)

Variables	D-I Cond.	Ti <sub>Mo</sub> (%TSN)	inc/coh <sub>Mo</sub>	PCA1 <sub>Mo</sub>	R <sub>850</sub> /R <sub>900</sub>	WSI-a %	WSI-b %	EDC-Na	EDC-TA	EDC CO <sub>2</sub>
D-I Cond.	<b>1</b>	-0.113	0.020	<b>0.041</b>	<b>0.192</b>	0.103	-0.014	<b>0.247</b>	0.037	0.129
Ti <sub>Mo</sub> (%TSN)		<b>1</b>	<b>-0.649</b>	<b>-0.721</b>	-0.044	0.064	0.059	0.083	0.102	0.061
inc/coh <sub>Mo</sub>			<b>1</b>	<b>0.910</b>	-0.174	0.040	0.010	-0.184	-0.046	0.025
PCA1 <sub>Mo</sub>				<b>1</b>	-0.147	0.082	0.034	-0.132	-0.054	-0.028
R <sub>850</sub> /R <sub>900</sub>					<b>1</b>	0.006	-0.036	0.106	0.154	-0.013
WSI-a %						<b>1</b>	-0.008	-0.025	0.056	0.099
WSI-b %							<b>1</b>	<b>0.202</b>	0.055	-0.001
EDC-Na								<b>1</b>	-0.146	-0.163
EDC-TA									<b>1</b>	0.084
EDC CO <sub>2</sub>										<b>1</b>

Values in bold are different from 0 with a significance level alpha=0.05; values shaded red(+) & blue(-) are significantly correlated (*p*<0.05)

p-values: Residuals (100-yr LOESS Interpolated)

Variables	D-I Cond.	Ti <sub>Mo</sub> (%TSN)	inc/coh <sub>Mo</sub>	PCA1 <sub>Mo</sub>	R <sub>850</sub> /R <sub>900</sub>	WSI-a %	WSI-b %	EDC-Na	EDC-TA	EDC CO <sub>2</sub>
D-I Cond.	<b>0</b>	0.248	0.841	0.675	<b>0.049</b>	0.293	0.887	<b>0.011</b>	0.709	0.187
Ti <sub>Mo</sub> (%TSN)		<b>0 &lt; 0.0001</b>	<b>&lt; 0.0001</b>		0.653	0.512	0.550	0.400	0.300	0.531
inc/coh <sub>Mo</sub>			<b>0 &lt; 0.0001</b>		0.075	0.683	0.918	0.059	0.640	0.803
PCA1 <sub>Mo</sub>				<b>0</b>	0.133	0.403	0.731	0.176	0.580	0.775
R <sub>850</sub> /R <sub>900</sub>					<b>0</b>	0.951	0.717	0.277	0.115	0.898
WSI-a %						<b>0</b>	0.935	0.798	0.570	0.313
WSI-b %							<b>0</b>	<b>0.038</b>	0.576	0.990
EDC-Na								<b>0</b>	0.135	0.095
EDC-TA									<b>0</b>	0.391
EDC CO <sub>2</sub>										<b>0</b>

Values in bold are different from 0 with a significance level alpha=0.05; values shaded red(+) & blue(-) are significantly correlated (*p*<0.05)

Notes: This Pearson correlation analysis of residuals quantifies the impact of serial autocorrelation. Residuals from the LOESS 2<sup>nd</sup> order polynomial smoothed 100-year intervals should be independent of the effects of serial autocorrelation; inc/coh<sub>Mo</sub> ( $\mu$ -XRF) has been used extensively as an organic proxy<sup>16</sup> and is included here as a control as it should remain positively correlated with PCA1 (as shown in Figure 2). D-I Cond refers to the Weighted Average Partial Least Squares Conductivity transfer function reconstruction shown in Figure 2. WSI is the winter sea ice proxy in PS2090, EDC-Na is EPICA Dome C Na-flux data; EDC-TA is EPICA Dome C Temperature Anomaly data; EDC-CO<sub>2</sub> is EPICA Dome C CO<sub>2</sub> data.

**Supplementary Table 6. Timing of phases of above- and below-mean wind-proxy data from Emerald Lake in calibrated years before present.** The timing of above (below) - mean phases is based on two or all three of the wind proxies being above (below) the 95% Upper bound mean: D-I conductivity=303  $\mu\text{S cm}^{-1}$ ; Ti/inc.+coh. =1.1% of TSN;  $R_{850}/R_{900}=0.97$ . The mean is represented by a solid blue line in Figure 2 (main text).

Above mean winds	Below mean winds
0 – 100	100 – 200
200 – 5,300	5,300 – 5,600
5,600 – 7,000	7,000 – 7,700
7,700 – 7,900	7,900 – 8,400
8,500 – 9,200	9,200 – 11,200
11,200 – 12,100	

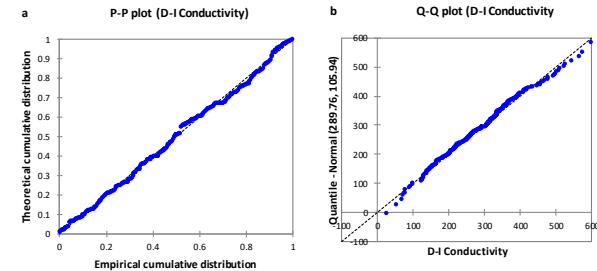
**Supplementary Table 7. Summary results of normality and autocorrelation tests for the Emerald Lake D-I conductivity dataset.**

D-I Conductivity (as measured dataset)							
	Shapiro-Wilk	Anderson-Dar.	Lilliefors test	Jarque-Bera			
W	0.993	$A^2$	0.429	D	0.039	Observed	2.06
				D (std)	0.618	Critical	
p-values	0.263	0.307	0.465	DF	5.99		2
H0 Rejection risks	26.32%	30.72%	46.46%				35.68%

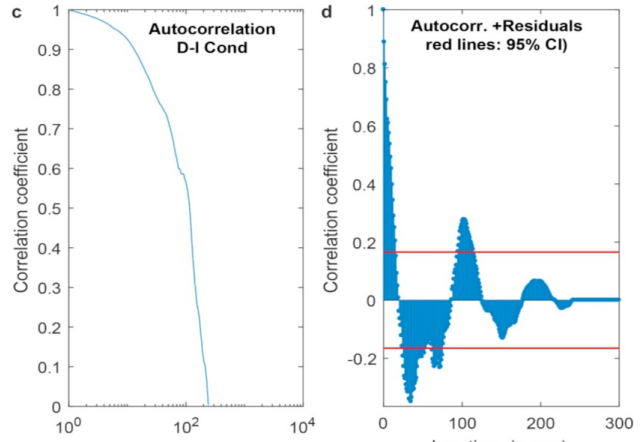
Computed p-value is greater than the sig. level alpha=0.05, accept the null hypothesis H0.

H0: The sample follows a Normal distribution.

Ha: The sample does not follow a Normal distribution.



D-I Conductivity (50-yr interpolated dataset)



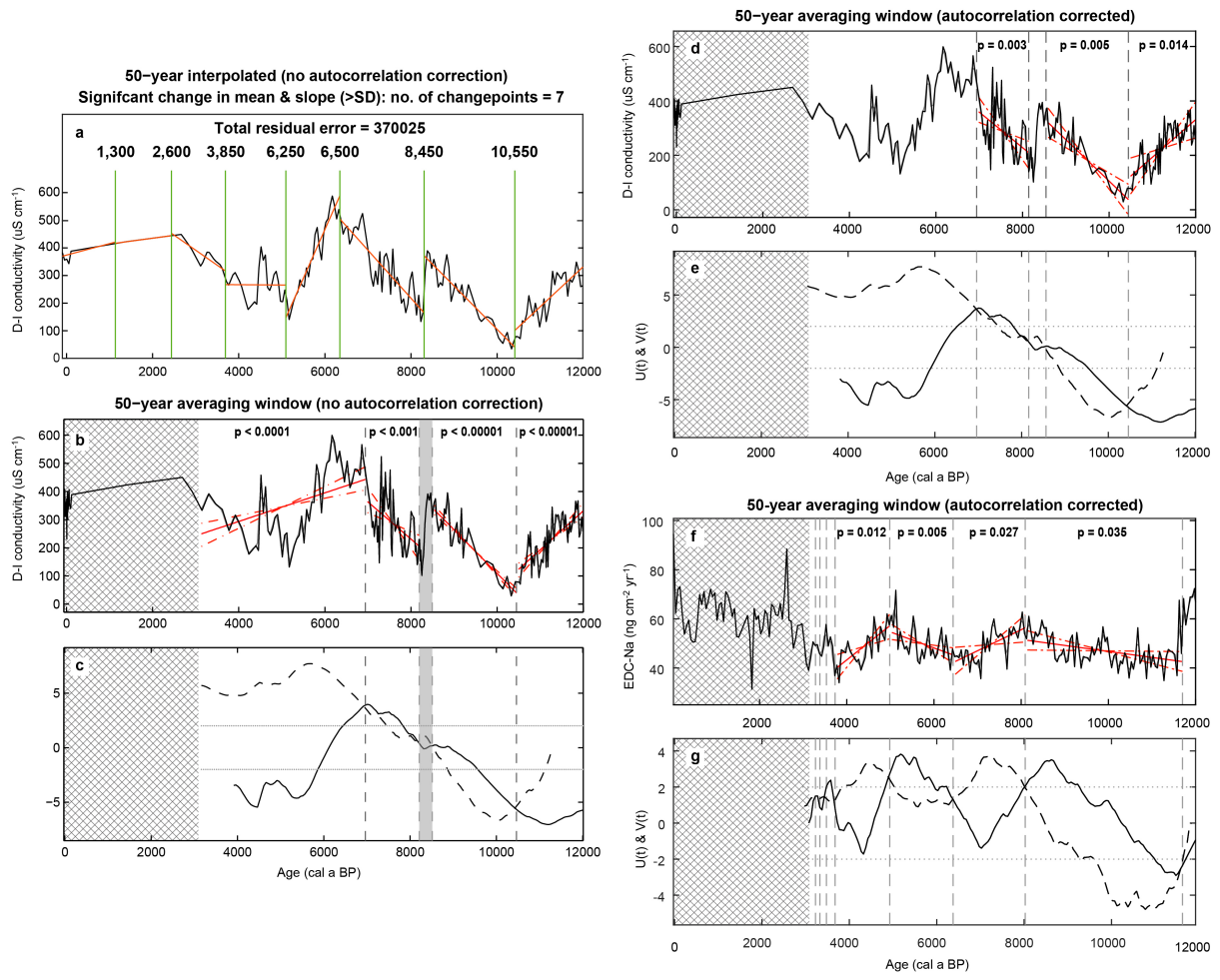
Notes: All other as-measured, log-transformed and natural-log transformed datasets failed S-W, Lillefors and J-B normality tests. All datasets examined were autocorrelated to a similar extent or greater than the D-I conductivity dataset.

### *Trends in wind proxy data from time-series analysis*

To explore potential relationships in trends between wind proxy data and the ice and marine core data, we undertook further tests of all time-series including autocorrelation and trend-change series analysis using Sequential Mann-Kendall Trend (SMKT) analysis (Supplementary Fig. 12; Supplementary Table 7, 8), without and with correction for serial autocorrelation, coupled with cross-spectral and cross-wavelet spectral coherence analysis (correction for serial autocorrelation included). Analysis was undertaken in XLStat and MATLAB following established methods refs<sup>38-40</sup> (Supplementary Fig. 13).

In summary, standard mean and slope change point and SMKT<sup>41,42</sup> analysis were used to determine the periods when significant trend changes occurred in each dataset. For a given time series  $X(t)$ , where  $t$  is the time from 1, 2, 3, ... to  $n$ , the SMKT calculates the progressive and retrograde ranking series  $U(t)$  and  $V(t)$ , which are functions of the expected values and the variance of the sequential subseries starting from the two ends of  $X(t)$  (i.e.  $X(1)$  and  $X(n)$ ). The temporal locations where  $U(t)$  and  $V(t)$  cross each other are used to identify the potential trend change points (Supplementary Fig. 12b, d). If the absolute values of either  $U(t)$  or  $V(t)$  become greater than 2 before and after a crossing point, the null hypothesis that  $X(t)$  has no trend change during this period is rejected. The statistical significance of the linear trends for individual subsections was then estimated by using the non-parametric Mann-Kendal Tau-Sens slope test<sup>43</sup> with a correction for autocorrelation. The code used by ref.<sup>44</sup> was adapted and executed in MathWorks Matlab® v. 2017b.

Without correction for autocorrelation, SMKT analysis reveals four significant ( $p \leq 0.05$ ) trend change points in the 50-yr averaged 4–12 ka D-I conductivity dataset (mean=44-year as-measured interval). The inclusion of a correction for serial autocorrelation reduces the number of significant trend change points to three, at c. 10,500, 8,600, 8,200 and 7,000 cal yr BP (Supplementary Fig. 12d; Supplementary Table 8a). The change points at c. 8,600, 8,200 and 7,000 cal yr BP are broadly consistent with significant changes in trend in the EDC Na<sup>+</sup> flux record at c. 8,000 and 6,400 years (i.e., within dating errors of c. 500-700 years). After correction for serial autocorrelation, both the 10-year and 50-yr averaged 4-12 ka Ti-datasets have only one significant change in trend, at c. 4,800 cal yr BP (not shown), which is similar in timing to a significant change in trend at c. 4,950 cal yr BP in the autocorrelation-corrected EDC Na<sup>+</sup> flux dataset (Supplementary Fig. 12f; Supplementary Table 8c, e). The  $R_{850}/R_{900}$  4–12 ka dataset has no significant changes in trend, with or without correction for serial autocorrelation.



**Supplementary Figure 12. Summary results of Change point and Sequential Mann-Kendall (SMKT) change point and trend time series analysis.** **a.** Mean and slope changepoint analysis using the whole-dataset standard deviation as the changepoint threshold value. **b-c.** SMKT analysis of 50-year averaged D-I conductivity data from Emerald Lake without correction for autocorrelation. **d-e.** SMKT analysis of 50-year averaged D-I conductivity data from Emerald Lake corrected for serial autocorrelation. **f-g.** SMKT analysis of 50-year averaged EDC-Na<sup>+</sup> flux data corrected for serial autocorrelation. The cross-hatched area was excluded from SMKT analysis due to a lack of data points. This was caused by a significant reduction in sediment accumulation in Emerald Lake from at least c. 3,000 years to the start of the C20<sup>th</sup>. In **a.**, Significant change points in the mean and slope of the D-I conductivity data are shown by green line, with age in years at the top, with the red line representing the linear trend of each section. For **b**-SMKT trend change points detected are shown as solid vertical or dashed grey lines with Age (cal yr BP). Solid red lines in **b, d, f** are the linear trends which are statistically significant at the  $p \leq 0.05$  level, with the 95% confidence intervals shown as dashed red lines (Supplementary Table 8). A 50-year average window, which is greater than the mean sampling resolution the diatom inferred (D-I) conductivity dataset is applied before the SMKT. The corresponding progressive and retrograde ranking series U(t) (solid) and V(t) (dashed) estimated by the SMKT are shown in **c, e, g** where the crossing points of U(t) and V(t) reflect the periods where significant changes in trend occurred. The dashed vertical grey lines in the conductivity profile indicate where possible changes in trend occur, which are indicated by U(t) and V(t) nearly crossing during those periods.

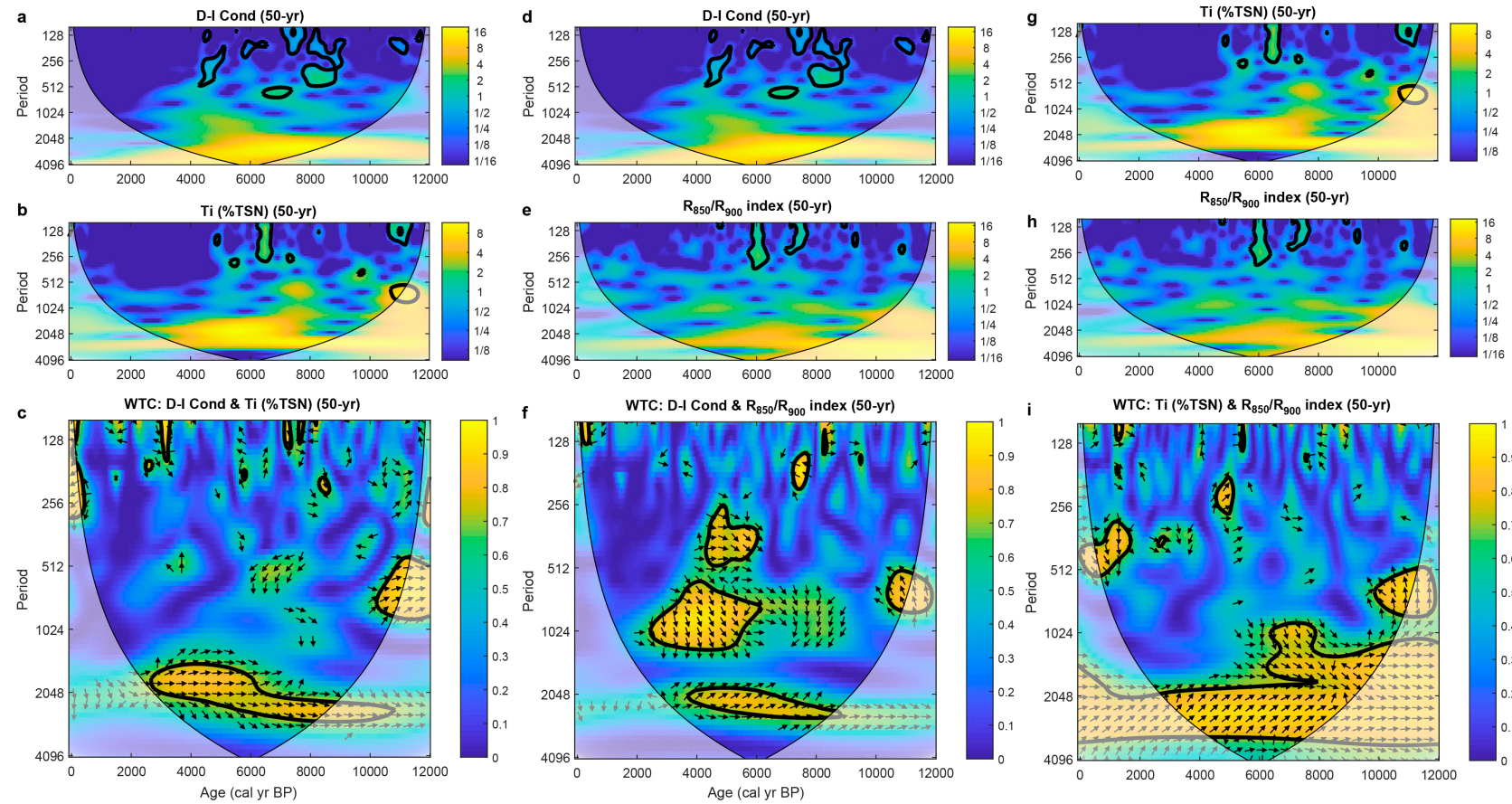
**Supplementary Table 8. Summary statistics for autocorrelation-corrected Sequential Mann-Kendall Test (SMKT) analysis.**

Changepoint location	Approximate Age (cal yr BP)	Tau-b Values	Tau Values	Lower 95% Conf. Band of the Trend	Average Trend	Upper 95% Conf. Band of the Trend	Significance of the trend	Linear Correlation Coefficient	p value of the Linear Correlation	Section Mean	Variance	Standard Deviation
<b>a) D-I Conductivity (3-12 kcal yr BP; 50 yr average resolution)</b>												
79	6990	-0.435	-0.435	-11.380	-6.539	-3.025	0.0032	-0.625	0.0011	288.4	4856	69.7
103	8190	0.571	0.571	-2.952	31.178	58.858	0.0635	0.828	0.0112	290.5	7836	88.5
111	8590	-0.815	-0.815	-10.588	-7.645	-4.672	0.0054	-0.951	<0.00001	182.5	7908	88.9
149	10490	0.652	0.652	2.465	6.934	11.296	0.0143	0.871	<0.00001	227.4	5205	72.1
<b>b) SPECIM R<sub>850</sub>/R<sub>900</sub> index (3-12 kcal yr BP; 50 yr average resolution)</b>												
0	0	-0.345	-0.345	-0.001	-0.001	0.000	0.0449	-0.452	<0.00001	0.977	0.003	0.052
<b>c) Ti/inc.+coh. (as % of TSN) (3-12 kcal yr BP; 50-yr average resolution)</b>												
0	0	0.375	0.375	-0.001	0.004	0.012	0.1056	0.551	0.0009	1.53	0.01	0.08
36	4840	-0.139	-0.139	-0.005	-0.002	0.002	0.2885	-0.089	0.2881	1.12	0.10	0.31
<b>d) WSI (800 years to 12 kcal yr BP) 100 year average resolution (original data resolution)</b>												
0	0	-0.538	-0.538	-0.680	-0.338	0.019	0.0674	-0.826	<0.00001	27.0	218.9	14.8
<b>e) EDC-Na (0-12 kcal yr BP; 50-yr average resolution)</b>												
0	0	0.600	0.600	-1.771	1.016	3.789	0.1329	0.666	0.1484	45.9	12.0	3.5
6	3250	-1	-1	-	-2.251	-	-	-1	-	46.6	1.3	1.1
8	3350	1	1	-	3.158	-	0.2963	0.887	0.3060	51.1	8.5	2.9
11	3500	-1	-1	-	-4.041	-	0.0894	-0.953	0.0468	46.0	25.0	5.0
15	3700	0.567	0.567	0.265	0.705	1.096	0.0119	0.802	<0.00001	48.7	35.8	6.0
40	4950	-0.369	-0.369	-0.558	-0.326	-0.120	0.0052	-0.592	0.0007	49.9	26.9	5.2
69	6400	0.549	0.549	0.067	0.428	0.754	0.0267	0.785	<0.00001	49.5	30.2	5.5
102	8050	-0.335	-0.335	-0.233	-0.122	-0.009	0.0351	-0.460	<0.00001	47.0	25.3	5.0
174	11650	0.600	0.600	-1.787	1.628	3.904	0.1329	0.782	0.0661	65.8	11.5	3.4
<b>f) EDC-Na (0-12 kcal yr BP) 50 year average from 1 yr data (original resolution)</b>												
0	0	-0.347	-0.347	-0.118	-0.063	-0.005	0.0354	-0.480	<0.00001	51.8	70.3	8.4
<b>g) Macquarie Island annual monthly average wind speed data (5-year moving average)</b>												
0	0	0.604	0.604	0.031	0.116	0.221	0.03160744	0.844	0.0001	9.27	0.41	0.64

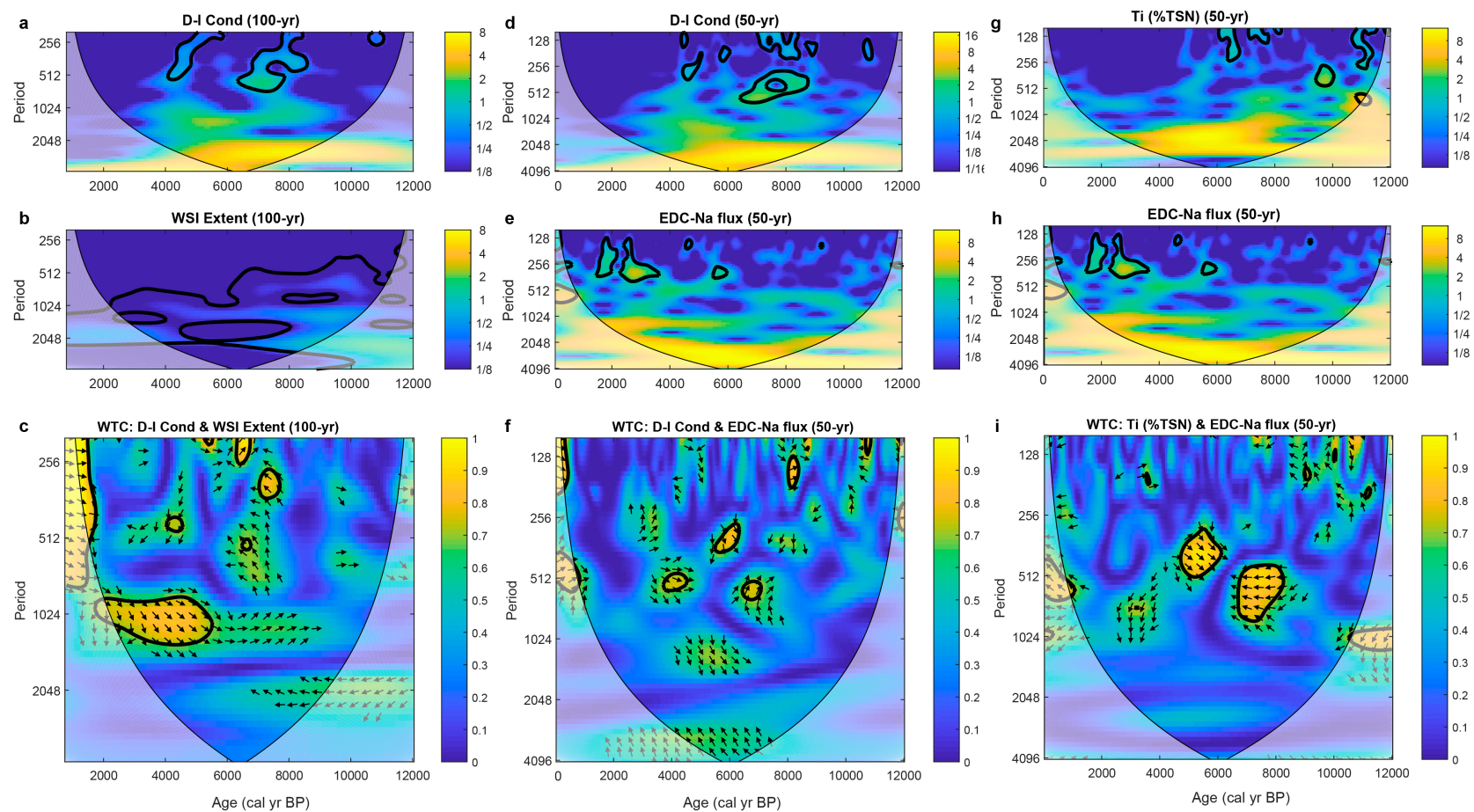
Notes: SMKT was applied to all datasets shown in Figures 2 and 3 (EDC Temperature and EDC CO<sub>2</sub> results not shown for clarity) and Macquarie Island 5-year moving average of average monthly wind speed data between 1948–2018 CE.

Wavelet and cross-wavelet coherence analysis revealed patchy phases of cyclicity exist in the conductivity, titanium and  $R_{850}/R_{900}$  index 50-year averaged datasets (Supplementary Fig. 13). There is some evidence of significant cycles with centennial-scale periodicity (c. 100–250 years and c. 250–500 years) in the conductivity record between c. 6,000–9,000 years (Supplementary Fig. 13d). Meanwhile the EDC-Na flux record has a significant centennial-scale periodicity between 2,000–4,000 years (Supplementary Fig. 14e).

Overall, we found no persistently significant or strong cross-spectral coherence between the wind proxy datasets over the last 12,000 years or between the wind proxies and the WSI extent or EDC-Na flux datasets (Supplementary Fig. 13c,f; Supplementary Figure 14c,f). However, the conductivity and Ti data have a strong and significant correlation with a c. 2000-year periodicity, which extends for most of the well-dated part of the Emerald Lake core from c. 3,000-c. 11,000 years, with a significant c. 500-year periodicity between c. 11,000–12,000 years (Supplementary Fig. 13c). The  $R_{850}/R_{900}$  index is significantly correlated with the conductivity record between c. 5,000–2,000 years at a millennial scale periodicity, and between 4,000–8,000 years at a multi-millennial scale periodicity, in a similarly positive direction (Supplementary Fig. 13f). Ti and  $R_{850}/R_{900}$  are significantly (positively) correlated at multi-millennial timescales (c. 2-5 kyrs) throughout the entire 12,000-year record (Supplementary Fig. 13i), and their millennial-scale periodicities do not change significantly if the time-averaging window is reduced to 10 years (although modelled dating errors are larger, the maximum measured mean resolution of the  $\mu$ -XRF dataset is c. 11 years). The conductivity and WSI records show a significant correlation, with a c. 1,000-year periodicity, between c. 2,000–5,000 years ago, corresponding to the persistently elevated conductivity levels and above average winter sea-ice extent over the last 12,000 years (Supplementary Fig. 14 a, b). The Ti and EDC-Na flux data have a significant and strong correlation with a centennial-millennial scale periodicity between c. 5000–8000 years, but are inversely correlated at around c. 5000 years (c. 250–500 periodicity) and c. 7000 years (c. 500–1000 periodicity) (Supplementary Fig. 14g-i).



**Supplementary Figure 13. Wavelet and Cross-spectral coherence analysis on new wind proxy data from Emerald Lake.** **a-c.** D-I conductivity and Ti datasets. **d-f.** D-I conductivity and  $R_{850}/R_{900}$  index datasets. **g-i.** Ti and  $R_{850}/R_{900}$  index datasets. Solid black lines represent areas of significant ( $p<0.05$ ) periodicity (years, left axes) in a,b,d,e,g,h and significant cross-coherence in c and f. Blue-yellow gradient represents areas of increasingly stronger cyclicity in a,b,d,e,g,h and increasingly stronger coherence in c,f,i. All records are 50-year averaged windows from -63–12,000 cal yr BP datasets.



**Supplementary Figure 14. Wavelet and Cross-spectral coherence analysis between key new wind proxy data and published datasets.**  
**a-c.** D-I conductivity and WSI datasets (100-year average window from 800–12,000 cal yr BP datasets). **d-f.** D-I conductivity and EDC-Na<sup>+</sup> flux datasets (50-year average window from 25–12,000 cal yr BP datasets). **g-i.** Ti (%TSN) and EDC-Na<sup>+</sup> flux datasets (50-year average window from 25–12,000 cal yr BP datasets).

### **Supplementary Note 6: The influence of lake ice cover and relative sea level change on aerosol inputs**

Lakes on Macquarie Island have not been observed to freeze completely, although up to 10 cm of ice cover has been occasionally observed on some small ponds<sup>1</sup>. During the Last Glacial temperatures are estimated to have been about 4–6 °C colder than today, similar to those on Macdonald Island, which remains free of permanent ice and snow cover<sup>1</sup>. It is possible that seasonal lake ice cover was more persistent during the late part of the LGIT. This would limit evaporation from the lakes in winter resulting in lower diatom-inferred conductivities. However, because the highest diatom-inferred conductivities were measured during the Late Glacial this process was likely of minor to transitory importance.

Changes in relative sea level from isostatic processes and tectonic uplift could all influence the relative distance of the lake from the coast (and hence delivery of sea salt aerosols) through time. Isostatic processes can be ruled out as Macquarie Island was not glaciated during the Last Glacial<sup>2</sup>. The tectonic uplift rate has been estimated at 0.8 mm yr<sup>-1</sup><sup>45</sup>, which equates to 80 cm per 1000 years. Based on these data the vertical displacement of the lake relative to the sea will have changed by less than 10 m through the Holocene. Relative sea level can also be discounted because the present-day relationship between altitude and conductivity of all plateau lakes is not significant ( $R^2=0.034$ ,  $n=30$ ) even though their altitudes range from 50–300 m a.s.l. The relationship between altitude and conductivity of the plateau lakes within 2.5 km from the coast is also not significant ( $R^2=0.263$ ,  $n=14$ ). This is because sea salts continue to be scavenged from the air as moisture and salt-laden air masses rise over the island and cool.

### **Supplementary Note 7: Comparison of the Macquarie Island wind reconstruction with other records**

In this study, we focus on reconstructing changes in the relative strength of the SHW over the core jets of the Antarctic Circumpolar Current, 50–55°S. We compare these with recent compilations of SHW dynamics from 41–50 °S<sup>46,47</sup>, to identify any zonally symmetric behaviour. There are relatively few records of the SHW between 50–55°S latitudes with good chronological control (defined here as having a mean of at least one age constraint per thousand years), which limits resolution at centennial to millennial time scales<sup>47</sup>. In relation to comparisons with southern South American sites, we restrict our discussion to studies on the western side of the Andes, as proxies that use the relationship between precipitation and the SHW are more straightforward than on the eastern side<sup>48,49</sup>.

Our study is the first wind reconstruction based on changes in sea salt and mineralogenic aerosol transport. Previously most studies at continental sites north of 55°S have relied on sub-fossil pollen analyses in peat and lake sediments. These depend on understanding the relationship between pollen assemblages and rainfall, and the site specific correlations between rainfall and SHW in meteorological records<sup>48</sup> (see discussions in Browne et al.<sup>50</sup>, Fletcher and Moreno<sup>51</sup>, Kilian and Lamy<sup>49</sup>, Moreno et al.<sup>47</sup>). There are a limited number of palynological records from sub-Antarctic islands (e.g. McGlone<sup>52</sup>, McGlone et al.<sup>53</sup>, Van der Putten et al.<sup>54</sup>, Strother et al.<sup>55</sup>). Some of these use changes in the supply of exotic pollen as a marker for changes in the SHW, but in all cases the exotic pollen concentrations are very low. Similarly, a lack of species diversity in the vegetation communities has resulted in diverging conclusions about how to infer climate history from pollen data<sup>56</sup>.

Careful consideration is also needed when interpreting other proxies including geochemical data. For example, Fe in a marine record off the Chilean coast at 41°S has been used to

infer changes in the relative inputs of Fe-poor ‘Coastal Range’ and Fe-rich ‘Andean source’ rock in relation to rainfall<sup>57</sup>. In this case increased Fe values were interpreted as indicating less humid conditions and more poleward located storm tracks<sup>57</sup>. Fe (as a ratio with Al, Fe/Al) in fjord sediments at 46°S has also been used with Ti/Al to infer changes in grain size, where greater Fe/Al values are interpreted as a decrease in seasonal floods due to a decrease in precipitation seasonality as a result of northward shifted SHW<sup>58</sup>. This demonstrates the importance of site-specific understanding of the behaviour of the proxies: Lamy et al.<sup>57</sup> related higher Fe values to less humid conditions, Bertrand et al.<sup>58</sup> related higher Fe values to more humid conditions year-round, both of which contrast the classical interpretation of Fe concentrations directly reflecting higher precipitation (e.g.<sup>59</sup>).

Varying interpretations of Holocene SHW behaviour have been published. Some records indicate a weak SHW in the early Holocene and strengthening towards the late Holocene, whereas others show the reverse pattern or do not reveal a clear trend<sup>49</sup>. There is some discussion ‘whether the SHW influence was anomalously high or low in south-western Patagonia during the early Holocene, and whether the core of the SHW shifted southward or whether its strength diminished’<sup>47</sup>. This extends to the mid-late Holocene where terrestrial ecosystem proxy records from western Patagonia<sup>60</sup> suggest a trend of increasing SHW strength over the last 7000 years that is not supported by sedimentological and pollen-based reconstructions of South Patagonian precipitation<sup>61</sup>. Some model simulations for this time period suggest opposite Holocene trends in SHW strength and position for different seasons, which may affect the proxy records and their interpretation<sup>62</sup>.

**12.1–11.2 ka BP:** One of the more consistent features amongst palaeo-records is a major shift in precipitation regimes at high southern latitudes (50°S southwards) at the start of the Holocene (Supplementary Fig. 15). This has been interpreted as a period of strong SHW in their core (50–55°S) across the Southern Hemisphere. Lamy et al.<sup>61</sup> combined records from 34–53°S on the western side of the Andes to infer strong SHW and wetter conditions at higher latitudes (53°S) at the start of the Holocene, while sites north of the main influence of the SHW (c. 34°S) experienced weaker winds and were drier. Moreno et al.<sup>60</sup> compared a site to the north of the core belt (41°S) to a site at 51°S to identify above average winds between c. 14–10.5 ka BP. Fletcher and Moreno<sup>46,51</sup> combined records from South America, Tasmania, New Zealand and southern Africa to infer enhanced SHW in these regions until c. 11 ka BP. Together with intensified winds at Macquarie Island this suggests a hemisphere-wide period of enhanced SHW at their core that extended northwards.

**11.2–9.2 ka BP:** The Macquarie Island record shows diminished SHW during the early Holocene 11.2–9.2 ka (Supplementary Fig. 15). This coincides with a number of studies in Tasmania and New Zealand indicating weaker winds from ca. 11–8 ka BP (Fletcher and Moreno<sup>46,51</sup>). Weaker winds were inferred by Moreno et al.<sup>60</sup> from ca. 10.5–7.8 ka BP for western Patagonia (51°S). Lamy et al.<sup>61</sup> used %Misodendron as a palaeoprecipitation indicator in Tamar Lake 1 (53°S). Misodendron is a hemiparasite that infests several Nothofagus species. Lamy et al.<sup>61</sup> interpreted the abundance of Misodendron in terms of the presence of open Nothofagus forest growing under limited ecological conditions (e.g. swamp soils), therefore indicating increased moisture availability and stronger winds, which was supported by their geochemical data<sup>61</sup>. However, Fletcher and Moreno<sup>51</sup> reinterpreted Lamy et al.’s Misodendron as reflecting a dry and open forest-steppe ecotone and therefore weaker winds during the early Holocene. Supplementary Fig. 15 illustrates these different SHW interpretations, where Fig. 15a and b show results from the present study, Fig. 15c shows the reinterpreted Misodendron record, while Fig. 15d,e illustrate the original geochemical data.

Taking the latter interpretation, we find that %Misodendron in Tamar Lake 1 is significantly inversely related to the Emerald Lake Ti data which we associate with wind strength ( $r=-0.65$ ;  $p<0.0001$ , Supplementary Fig. 15a,c). This suggests a potential hemisphere-wide period of weaker winds. Together with the start of the Holocene, which was characterised by strong winds, this indicates that periods of low (or high) relative wind strength at Macquarie Island correspond to periods of low (or high) precipitation and therefore relative wind strength in regions to the north (e.g., Tasmania, New Zealand and Southern Chile).

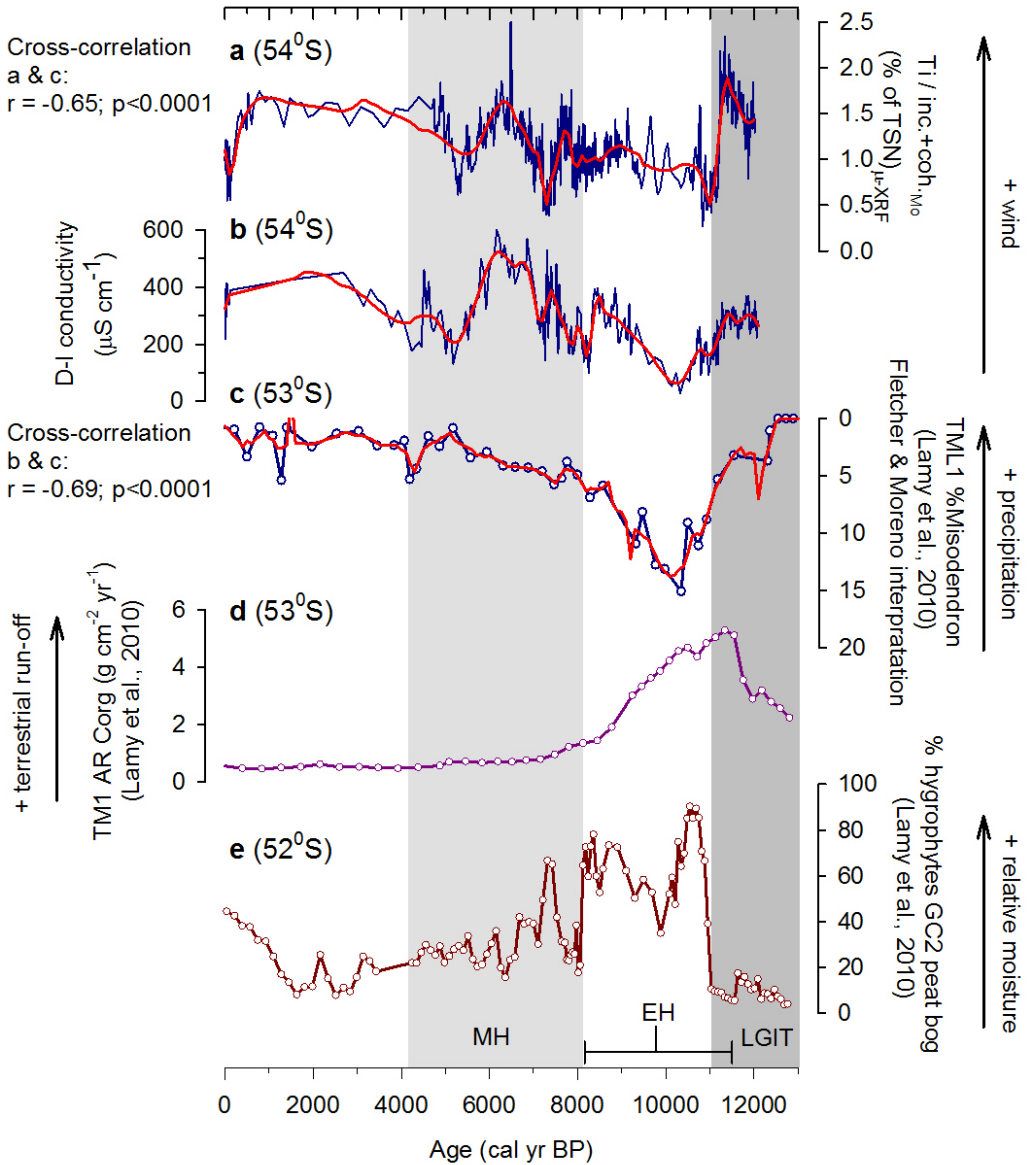
However, this interpretation is not consistent across all studies. Lamy et al.<sup>61</sup> inferred stronger winds from the start of the Holocene until ca. 8.5 ka BP (53°S, Figure 15d,e). This is based on higher organic carbon accumulation rates (AR Corg) in Tamar Fjord (TM1, Supplementary Fig. 15d) and greater %hydrophytes (GC, Supplementary Fig. 15e) from Gran Campo 2 peat bog (and the original interpretation of Misodendron in Tamar Lake 1). AR Corg and %hydrophytes are interpreted as palaeoprecipitation proxies (Supplementary Fig. 15d-e). A comparison of the Emerald Lake Ti data with hydrophyte abundance in the Gran Campo 2 peat bog shows there is a significant inverse relationship ( $r=-0.70$ ;  $p<0.0001$ , Supplementary Fig. 15a, e)<sup>61</sup>. Similarly, there is an inverse relationship with biogenic accumulation rates at the TM1 fjord site (Supplementary Fig. 15a, d)<sup>61</sup>. A recent study in Tasmania reconstructed high rainfall, irregular fires and increased charcoal flux between 11.5–8.3 ka BP, suggesting stronger SHW flow over the region (Rees et al. 2015).

If the interpretation of stronger winds in southern Chile at the same time as weaker winds at Macquarie Island is replicated in future studies, it would suggest key regional differences in SHW behaviour, where weaker winds at Macquarie Island and sites to the north (Tasmania and New Zealand) correspond with stronger winds in southern Chile around 53°S.

Whilst our data favour the hypotheses of diminished SHW in the early Holocene, more well-dated, multi proxy records are needed to distinguish changes in the intensity of the SHW from changes in latitudinal position. This should be possible with further records of the SHW in the sub-Antarctic region and a rigorous re-evaluation (and in some cases re-dating) of continental records. Similarly, more research is needed to constrain the evaporation side of the precipitation/evaporation balance (which is often unconstrained except in lake level reconstructions<sup>49</sup>.

**9.2–5.3 ka BP:** Our data suggest increased and higher amplitude changes in wind intensity occurred at Macquarie Island. The presence of windblown sand and stones in cliff edge peat profiles on Auckland Island (50°S, 640 km northeast of Macquarie Island) and Campbell Island (52°S, 700 km northeast of Macquarie Island) from c. 8 ka BP suggests strengthening westerlies<sup>52</sup>.

Wetter conditions and stronger winds (either due to overall strengthening or northward displacement of the SHW) are inferred in the western half of Tasmania from c. 9.2–5 ka BP<sup>46,51,63,72</sup>. Stronger winds were also identified at Isla de los Estados, Tierra del Fuego (55°S, <sup>64</sup>). Other records from Tierra del Fuego also suggest more humid conditions between c. 8–6 ka BP<sup>65,66</sup>. Some records have found evidence for intensifying SHW after 7.8 ka BP, which stabilised c. 6.8 ka BP<sup>60</sup>. Glacial records have found evidence of neoglacial advances c. 8.5 ka BP and 6.2 ka BP in central Patagonia at 46 °S<sup>67</sup>, and at 6.5 ka BP in New Zealand at 43 °S<sup>68</sup>, interpreted as likely a result of a northward migration of the SHW that caused an increase in precipitation and/or a decrease in temperature at this latitude. After 8.6 ka BP sea ice expanded around Antarctica. This may have caused a stronger temperature gradient and northward migration of the SHW, resulting in stronger winds both in their core belt and at sites further north (e.g. Lamy et al.<sup>57</sup>, Unkel et al.<sup>64</sup>).



**Supplementary Figure 15.** Comparison of Emerald Lake wind proxy data with selected Holocene records in the core belt of the SHW (50–55°S) with good chronological control (defined here as having a mean of at least one age constraint per thousand years). **a.** Emerald Lake Titanium (Ti). **b.** Emerald Lake diatom inferred conductivity. **c.** Relative pollen percentages of *Misodendron* in a core from Lake Tamar (Core TML1) interpreted as an indicator of a dry and open forest-steppe ecotone by Fletcher and Moreno<sup>46</sup> from an original study by Lamy et al.<sup>61</sup>. **d.** Terrestrial organic carbon flux into fjord Site TM1 as a recorder of fluvial supply<sup>61</sup>. **e.** Pollen percentage of hygrophytic taxa in the Gran Campo 2 (GC2) peat bog<sup>61</sup>. Red lines are 100-year interval 2<sup>nd</sup> order LOESS-smoothed data. Grey and white zones highlight periods discussed in the text. LGIT is Last Glacial-Interglacial Transition, EH is early Holocene, MH is mid Holocene, LH is late Holocene. The formal definition of the EH is denoted by the black horizontal bar.

**5.3–0 ka BP:** This period was characterised by relatively constant and intense winds at Macquarie Island since c. 5.3 ka BP. A pollen record from Fan Lake, South Georgia (54 °S) provides evidence of stronger SHW during the late Holocene<sup>55</sup>. In Patagonia, most glacier advances occurred after 5.5 ka BP, which were probably primarily driven by short term (a

few hundreds of years) increases in SHW strength and related increases in precipitation/accumulation<sup>49</sup>. Evidence from marine core records located around the coast of Antarctica and model outputs suggest an intensification of upwelling and wind stress during different seasons in the Southern Ocean from 5–3 ka BP<sup>69,70</sup>. This is consistent with our record suggesting more intense winds in the core belt of the SHW.

In contrast, Lamy et al.<sup>61</sup> found reduced precipitation and weaker westerlies compared to the early Holocene after 5.5 ka BP at 53 °S in Patagonia. This is consistent with a record from Isla de los Estados, Tierra del Fuego (55 °S) that found less precipitation and weaker winds occurred from 4.5 ka BP onwards<sup>64</sup>. Later, in New Zealand a shift from warm winters with wet summers to cooler winters and drier summers occurred c. 3.4 ka BP. This was attributed to stronger SHW flow in winter over southern New Zealand and stronger El Niño Southern Oscillation variations<sup>71</sup>. Decreased SHW strength from c. 4–1.6 ka BP and stronger winds from c. 1.6–0.9 ka BP together with geochemical data in a fjord on Auckland Island have also been reported<sup>50</sup>.

Changes in the relative influence of the SHW have been identified in western Tasmania, where decreased moisture availability and increased fire activity have been linked to increasingly frequent El Niño events in the tropical Pacific (e.g. Beck et al.<sup>72</sup>; Mariani et al.<sup>63</sup>; Fletcher et al.<sup>73</sup>; Rees et al.<sup>74</sup>), rather than a climate dominated by the SHW<sup>51</sup>. In southwestern Tasmania, Fletcher et al. recently identified synchronous and in-phase centennial-scale trends between their rainfall and fire activity records with records from southern South America. They also identified covariance between their record and Antarctic ice core CO<sub>2</sub><sup>79</sup>. As is the case with the early Holocene, these differing interpretations indicate the need for further well dated, multi proxy records to understand past SHW behaviour (strength and latitudinal position) within and between regions.

#### **Supplementary Note 8: Other data Sources**

Processed data for Figure 1 (file: blended\_seawinds\_1995-2005\_absolute\_windspeed.asc, blended\_seawinds\_1995-2005.tif) is deposited in the Natural Environment Research Council Polar Data Centre:

<https://www.bas.ac.uk/data/uk-pdc/>

These datasets contain the 11-year climatological monthly means (1995–2005) plotted on a 0.25 degree grid. The values are absolute wind-speed, calculated from the U and V vectors, in ms<sup>-1</sup>. No wind direction information is included in this raster. The original data was downloaded from:

<https://www.ncdc.noaa.gov/data-access/marinocean-data/blended-global/blended-sea-winds>

<ftp://eclipse.ncdc.noaa.gov/pub/seawinds/SI/uv/clm/>.

Average monthly wind speed data measured at 8 m a.s.l. at Macquarie Island base and upper atmosphere data for the period 1948–2018 CE was downloaded from the BAS-READER website:

<https://legacy.bas.ac.uk/met/READER/>

<https://legacy.bas.ac.uk/met/READER/surface/stationwind.html>

[https://legacy.bas.ac.uk/met/READER/upper\\_air/uawind.html](https://legacy.bas.ac.uk/met/READER/upper_air/uawind.html)

Data for ss-Na, were obtained from Röthlisberger et al.<sup>75,76</sup>

[ftp://ftp.ncdc.noaa.gov/pub/data/paleo/icecore/antarctica/epica\\_domec/edc-ca-na.txt](ftp://ftp.ncdc.noaa.gov/pub/data/paleo/icecore/antarctica/epica_domec/edc-ca-na.txt)).

Data for temperature were obtained from Jouzel et al.<sup>77</sup>

[ftp://ftp.ncdc.noaa.gov/pub/data/paleo/icecore/antarctica/epica\\_domec/edc3deuttemp2007.txt](ftp://ftp.ncdc.noaa.gov/pub/data/paleo/icecore/antarctica/epica_domec/edc3deuttemp2007.txt).

Data for CO<sub>2</sub> were obtained from Monnin et al.<sup>78</sup>

[ftp://ftp.ncdc.noaa.gov/pub/data/paleo/icecore/antarctica/epica\\_domec/edc-co2.txt](ftp://ftp.ncdc.noaa.gov/pub/data/paleo/icecore/antarctica/epica_domec/edc-co2.txt)).

Data for Southern Ocean winter sea ice extent was derived from Xiao et al.<sup>35</sup> and Ferry et al.<sup>36</sup> [https://data.aad.gov.au/metadata/records/ASAC\\_2534\\_winter\\_sea\\_ice](https://data.aad.gov.au/metadata/records/ASAC_2534_winter_sea_ice)

The spectral analysis software used to analyse data were downloaded from:

<https://www.marum.de/Michael-Schulz/Michael-Schulz-Software.html>

## References

- 1 Selkirk, P. M., Seppelt, R. D. & Selkirk, D. R. *Subantarctic Macquarie Island: Environment and Biology*. (Cambridge University Press, 1990).
- 2 Hodgson, D. A. et al. Terrestrial and submarine evidence for the extent and timing of the Last Glacial Maximum and the onset of deglaciation on the maritime-Antarctic and sub-Antarctic islands. *Quaternary Science Reviews* **100**, 137-158 (2014).
- 3 Australian-Government-Bureau-of-Meteorology. *Climate statistics for Australian locations, Macquarie Island*, <[http://www.bom.gov.au/climate/averages/tables/cw\\_300004\\_All.shtml](http://www.bom.gov.au/climate/averages/tables/cw_300004_All.shtml)> (2017).
- 4 Holloway, M. D., Sime, L. C., Singarayer, J. S., Tindall, J. C. & Valdes, P. J. Reconstructing paleosalinity from δ<sup>18</sup>O: Coupled model simulations of the Last Glacial Maximum, Last Interglacial and Late Holocene. *Quaternary Science Reviews* **131, Part B**, 350-364, doi:<http://dx.doi.org/10.1016/j.quascirev.2015.07.007> (2016).
- 5 Saunders, K. M. et al. Ecosystem impacts of feral rabbits on World Heritage sub-Antarctic Macquarie Island: A palaeoecological perspective. *Anthropocene* **3**, 1-8 (2013).
- 6 Buckney, R. T. & Tyler, P. A. Reconnaissance limnology of subantarctic islands.11. Additional features of the chemistry of Macquarie Island lakes and tarns. *Australian Journal of Marine and Freshwater Research* **25**, 89 - 95 (1974).
- 7 Bronk Ramsey, C. Bayesian analysis of radiocarbon dates. *Radiocarbon* **51**, 337-360 (2009).
- 8 Hogg, A. et al. SHCal13 Southern Hemisphere Calibration, 0-50,000 years cal BP. *Radiocarbon* **55**, 1889-1903 (2013).
- 9 Hua, Q., Barbetti, M. & Rakowski, A. Z. Atmospheric radiocarbon for the period 1950-2010. *Radiocarbon* **55**, 1-14 (2013).
- 10 Reimer, P. J. et al. Intcal04 Terrestrial Radiocarbon Age Calibration, 0-26 Cal kyr BP. *Radiocarbon* **46**, 1029-1058 (2004).
- 11 Reimer, P. J. et al. IntCal13 and Marine13 Radiocarbon Age Calibration Curves 0–50,000 Years cal BP. *Radiocarbon* **55**, 1869-1887, doi:10.2458/azu\_js\_rc.55.16947 (2013).
- 12 Blaauw, M. Methods and code for 'classical' age-modelling of radiocarbon sequences. *Quaternary Geochronology* **5**, 512-518 (2010).
- 13 Blaauw, M. & Christen, J. A. Flexible paleoclimate age-depth models using an autoregressive gamma process. 457-474, doi:10.1214/ba/1339616472 (2011).
- 14 Rioja: Analysis of Quaternary Science Data, R package version (0.9-3) (2014).
- 15 Suzuki, R. & Shimodaira, H. Pvclust: an R package for assessing the uncertainty in hierarchical clustering. *Bioinformatics* **22**, 1540-1542 (2006).

- 16 Davies, S. J., Lamb, H. F. & Roberts, S. J. in *Micro-XRF Studies of Sediment Cores, Developments in Palaeoenvironmental Research series*, (eds Croudace IW & Rothwell RG) (Springer, 2015).
- 17 Kylander, M. E., Ampel, L., Wohlfarth, B. & Veres, D. High-resolution X-ray fluorescence core scanning analysis of Les Echets (France) sedimentary sequence: new insights from chemical proxies. *Journal of Quaternary Science* **26**, 109-117 (2011).
- 18 Kylander, M. E., Lind, E. M., Wastegård, S. & Löwemark, L. Recommendations for using XRF core scanning as a tool in tephrochronology. *The Holocene* **22**, 371-375 (2012).
- 19 Roberts, S. J. *et al.* Past penguin colony responses to explosive volcanism on the Antarctic Peninsula. *Nature Communications* doi:10.1038/ncomms14914 (2017).
- 20 Boyle, J. F., Chiverrell, R. C. & Schillereff, D. in *Micro-XRF Studies of Sediment Cores: Applications of a non-destructive tool for the environmental sciences* (eds Ian W. Croudace & R. Guy Rothwell) 373-390 (Springer Netherlands, 2015).
- 21 C2 Version 1.5. Software for ecological and palaeoecological data analysis and visualisation (Newcastle University, 2007).
- 22 Paillard, D., Labeyrie, L. & Yiou, P. Macintosh program performs time-series analysis. *Eos, Washington. DC* **77**, 379 (1996).
- 23 Rioja v. 0.5-6 (<http://www.staff.ncl.ac.uk/staff/stephen.juggins/>, 2009).
- 24 Schmale, J. *et al.* Sub-Antarctic marine aerosol: dominant contributions from biogenic sources. *Atmos. Chem. Phys.* **13**, 8669-8694, doi:10.5194/acp-13-8669-2013 (2013).
- 25 Croome, R. Limnological studies on Macquarie Island *Tasmanian Field Naturalist* **78**, 26-27 (1984).
- 26 Mallis, M. A quantitative investigation of aerosol (salt) scavenging on Macquarie Island. *Papers and Proceedings of the Royal Society of Tasmania* **122**, 121-128 (1988).
- 27 Saunders, K. M., Hodgson, D. A. & McMinn, A. Quantitative relationships between benthic diatom assemblages and water chemistry in Macquarie Island lakes and their potential to reconstruct past environmental changes. *Antarctic Science* **21**, 35-49, doi:10.1017/S0954102008001442 (2009).
- 28 Van Nieuwenhuyze, W. *Reconstruction of Holocene paleoenvironmental changes in the sub-Antarctic region* PhD thesis, University of Ghent, (2015).
- 29 Heimburger, A., Losno, R., Triquet, S. & Nguyen, E. B. Atmospheric deposition fluxes of 26 elements over the Southern Indian Ocean: Time series on Kerguelen and Crozet Islands. *Global Biogeochemical Cycles* **27**, 440-449, doi:10.1002/gbc.20043 (2013).
- 30 Metcalfe, S. E., Jones, M. D., Davies, S. J., Noren, A. & MacKenzie, A. Climate variability over the last two millennia in the North American Monsoon region, recorded in laminated lake sediments from Laguna de Juanacatlán, Mexico. *The Holocene* **20**, 1195-1206 (2010).
- 31 Löwemark, L. *et al.* Normalizing XRF-scanner data: A cautionary note on the interpretation of high-resolution records from organic-rich lakes. *Journal of Asian Earth Sciences* **40**, 1250-1256 (2011).
- 32 Croudace, I. W., Rindby, A. & Rothwell, R. G. in *New Techniques in Sediment Core Analysis* (ed R.G. Rothwell) 51-63 (2006).
- 33 Butz, C. *et al.* Hyperspectral imaging spectroscopy: A promising method for the biogeochemical analysis of lake sediments. *J. Appl. Remote Sens.* **9**, doi:10.1117/1111.JRS.1119.096031 (2015).
- 34 Rein, B. & Sirocko, F. In-situ reflectance spectroscopy – analysing techniques for high-resolution pigment logging in sediment cores. *International Journal of Earth Sciences* **91**, 950-954, doi:10.1007/s00531-002-0264-0 (2002).
- 35 Xiao, W., Esper, O. & Gersonde, R. Last Glacial - Holocene climate variability in the Atlantic sector of the Southern Ocean. *Quaternary Science Reviews* **135**, 115-137, doi:<http://dx.doi.org/10.1016/j.quascirev.2016.01.023> (2016).

- 36 Ferry, A. J. et al. First records of winter sea ice concentration in the southwest Pacific sector of the Southern Ocean. *Paleoceanography* **30**, 1525-1539, doi:10.1002/2014PA002764 (2015).
- 37 Rehfeld, K. & Kurths, J. Similarity estimators for irregular and age-uncertain time series. *Clim. Past* **10**, 107-122, doi:10.5194/cp-10-107-2014 (2014).
- 38 Grinsted, A., Moore, J. C. & Jevrejeva, S. Application of the cross wavelet transform and wavelet coherence to geophysical time series. *Nonlinear Processes in Geophysics* **11**, 561-566, doi:10.5194/npg-11-561-2004 (2004).
- 39 Schulz, M. & Mudelsee, M. REDFIT: estimating red-noise spectra directly from unevenly spaced paleoclimatic time series. *Computers & Geosciences* **28**, 421-426 (2002).
- 40 Turner, J. et al. Absence of 21st century warming on Antarctic Peninsula consistent with natural variability. *Nature* **535**, 411-415, doi:10.1038/nature18645 (2016).
- 41 Gerstengarbe, F. W. & Werner, P. C. Estimation of the beginning and end of recurrent events within a climate regime. *Climate Research* **11**, 97-107 (1999).
- 42 Mann, H. B. Non parametric test against trend. *Econometric* **13**, 245-259 (1945).
- 43 A non-parametric monotonic trend test computing Mann-Kendall Tau, Tau-b, and Sens Slope written in MathWorks MATLAB (King County, Department of Natural Resources and Parks, Science and Technical Services 2006).
- 44 Grinsted, A. & Dahl-Jensen, D. A Monte Carlo-tuned model of the flow in the NorthGRIP area. *Annals of Glaciology* **35**, 527-530 (2002).
- 45 Adamson, D. A., Selkirk, P. M., Price, D. M., Ward, N. & Selkirk, J. M. Pleistocene uplift and palaeoenvironments of Macquarie Island: evidence from palaeobeaches and sedimentary deposits. *Papers and Proceedings of the Royal Society of Tasmania* **130**, 25-32 (1996).
- 46 Fletcher, M.-S. & Moreno, P. I. Zonally symmetric changes in the strength and position of the Southern Westerlies drove atmospheric CO<sub>2</sub> variations over the past 14 k.y. *Geology DOI: 10.1130/G31807.1* (2011).
- 47 Moreno, P. I. et al. Onset and Evolution of Southern Annular Mode-Like Changes at Centennial Timescale. *Scientific Reports* **8**, 3458, doi:10.1038/s41598-018-21836-6 (2018).
- 48 Garreaud, R. D., Vuille, M., Compagnucci, R. & Marengo, J. Present-day South American climate. *Palaeogeography, Palaeoclimatology, Palaeoecology* **281**, 180-195, doi:<http://dx.doi.org/10.1016/j.palaeo.2007.10.032> (2009).
- 49 Kilian, R. & Lamy, F. A review of Glacial and Holocene paleoclimate records from southernmost Patagonia (49–55°S). *Quaternary Science Reviews* **53**, 1-23, doi:<http://dx.doi.org/10.1016/j.quascirev.2012.07.017> (2012).
- 50 Browne, I. M. et al. Late Holocene intensification of the westerly winds at the subantarctic Auckland Islands (51°S), New Zealand. *Clim. Past Discuss.* **2017**, 1-37, doi:10.5194/cp-2017-52 (2017).
- 51 Fletcher, M.-S. & Moreno, P. I. Have the Southern Westerlies changed in a zonally symmetric manner over the last 14,000 years? A hemisphere-wide take on a controversial problem. *Quaternary International* **253**, 32-46 (2012).
- 52 McGlone, M. S. The Late Quaternary peat, vegetation and climate history of the Southern Oceanic Islands of New Zealand. *Quaternary Science Reviews* **21**, 683-707 (2002).
- 53 McGlone, M. S., Turney, C. S. M., Wilmshurst, J. M., Renwick, J. & Pahnke, K. Divergent trends in land and ocean temperature in the Southern Ocean over the past 18,000 years. *Nature Geoscience DOI: 10.1038/NGEO931* (2010).
- 54 Van der Putten, N., Mauquoy, D., Verbruggen, C. & Björck, S. Subantarctic peatlands and their potential as palaeoenvironmental and palaeoclimatic archives. *Quaternary International* **268**, 65-76 (2012).
- 55 Strother, S. L. et al. Changes in Holocene vegetation, climate and the intensity of Southern Hemisphere Westerly Winds based on a high-resolution palynological record from sub-Antarctic South Georgia. *The Holocene* **25**, 263-279 (2015).

- 56 Van der Putten, N. et al. Is palynology a credible climate proxy in the Subantarctic? *The Holocene* **22**, 1113-1121, doi:10.1177/0959683612441804 (2012).
- 57 Lamy, F., Hebbeln, D., Rohl, U. & Wefer, G. Holocene rainfall variability in southern Chile: a marine record of latitudinal shifts of the Southern Westerlies. *Earth and Planetary Science Letters* **185**, 369-382 (2001).
- 58 Bertrand, S., Hughen, K., Sepúlveda, J. & Pantoja, S. in *Supplement to: Bertrand, S et al. (2014): Late Holocene covariability of the southern westerlies and sea surface temperature in Northern Chilean Patagonia. Quaternary Science Reviews*, 105, 195-208, doi:10.1016/j.quascirev.2014.09.021 (PANGAEA, 2014).
- 59 Sepúlveda, J. et al. Late Holocene sea-surface temperature and precipitation variability in northern Patagonia, Chile (Jacaf Fjord, 44°S). *Quaternary Research* **72**, 400-409, doi:<https://doi.org/10.1016/j.yqres.2009.06.010> (2009).
- 60 Moreno, P. I., François, J. P., Moy, C. M. & Villa-Martínez, R. P. Covariability of the Southern Westerlies and atmospheric CO<sub>2</sub> during the Holocene. *Geology* **38**, 727-730. doi: 710.1130/G30962.30961 (2010).
- 61 Lamy, F. et al. Holocene changes in the position and intensity of the Southern Westerly wind belt. *Nature Geoscience* **3**, 695-699 (2010).
- 62 Varma, V. et al. Holocene evolution of the Southern Hemisphere westerly winds in transient simulations with global climate models. *Clim. Past* **8**, 391-402, doi:10.5194/cp-8-391-2012 (2012).
- 63 Mariani, M. et al. How old is the Tasmanian cultural landscape? A test of landscape openness using quantitative land-cover reconstructions. *Journal of Biogeography* **44**, 2410-2420, doi:doi:10.1111/jbi.13040 (2017).
- 64 Unkel, I., Fernandez, M., Björck, S., Ljung, K. & Wohlfarth, B. Records of environmental changes during the Holocene from Isla de los Estados (54.4°S), southeastern Tierra del Fuego. *Global and Planetary Change* **74**, 99-113, doi:<https://doi.org/10.1016/j.gloplacha.2010.07.003> (2010).
- 65 Waldmann, N. et al. Holocene climatic fluctuations and positioning of the Southern Hemisphere westerlies in Tierra del Fuego (54° S), Patagonia. *Journal of Quaternary Science* **25**, 1063-1075, doi:doi:10.1002/jqs.1263 (2010).
- 66 Waldmann, N. et al. Integrated reconstruction of Holocene millennial-scale environmental changes in Tierra del Fuego, southernmost South America. *Palaeogeography, Palaeoclimatology, Palaeoecology* **399**, 294-309, doi:<http://dx.doi.org/10.1016/j.palaeo.2014.01.023> (2014).
- 67 Douglass, D. C. et al. Evidence of early Holocene glacial advances in southern South America from cosmogenic surface-exposure dating. *Geology* **33**, 237-240, doi:10.1130/G21144.1 (2005).
- 68 Schaefer, J. M. et al. High-Frequency Holocene Glacier Fluctuations in New Zealand Differ from the Northern Signature. *Science* **324**, 622-625, doi:10.1126/science.1169312 (2009).
- 69 Denis, D. et al. Sea ice and wind variability during the Holocene in East Antarctica: insight on middle–high latitude coupling. *Quaternary Science Reviews* **29**, 3709-3719, doi:<https://doi.org/10.1016/j.quascirev.2010.08.007> (2010).
- 70 Renssen, H., Goosse, H., Fichefet, T., Masson-Delmotte, V. & Koc, N. Holocene climate evolution in the high-latitude Southern Hemisphere simulated by a coupled atmosphere-sea ice-ocean-vegetation model. *The Holocene* **15**, 951-964, doi:10.1191/0959683605hl869ra (2005).
- 71 Wilmsurst, J. M., McGlone, M. S. & Charman, D. J. Holocene vegetation and climate change in southern New Zealand: linkages between forest composition and quantitative surface moisture reconstructions from an ombrogenous bog. *Journal of Quaternary Science* **17**, 653-666, doi:doi:10.1002/jqs.689 (2002).
- 72 Beck, K. K. et al. The indirect response of an aquatic ecosystem to long-term climate-driven terrestrial vegetation in a subalpine temperate lake. *Journal of Biogeography* **45**, 713-725, doi:doi:10.1111/jbi.13144 (2018).

- 73 Fletcher, M.-S. *et al.* Changes in biomass burning mark the onset of an ENSO-influenced climate regime at 42°S in southwest Tasmania, Australia. *Quaternary Science Reviews* **122**, 222-232, doi:<https://doi.org/10.1016/j.quascirev.2015.05.002> (2015).
- 74 Rees, A. B. H., Cwynar, L. C. & Fletcher, M.-S. Southern Westerly Winds submit to the ENSO regime: A multiproxy paleohydrology record from Lake Dobson, Tasmania. *Quaternary Science Reviews* **126**, 254-263, doi:<https://doi.org/10.1016/j.quascirev.2015.08.022> (2015).
- 75 Röthlisberger, R. in *Data Contribution Series #2005-046* (ed IGBP PAGES/World Data Center for Paleoclimatology) (NOAA/NGDC Paleoclimatology Program, Boulder CO, USA, 2005).
- 76 Röthlisberger, R. *et al.* Dust and sea salt variability in central East Antarctica (Dome C) over the last 45 kyrs and its implications for southern high-latitude climate. *Geophysical Research Letters* **29**, 24-21-24-24, doi:10.1029/2002GL015186 (2002).
- 77 Jouzel, J. *et al.* Orbital and Millennial Antarctic Climate Variability over the Past 800,000 Years. *Science* **317**, 793-796, doi:10.1126/science.1141038 (2007).
- 78 Monnin, E. *et al.* Atmospheric CO<sub>2</sub> Concentrations over the Last Glacial Termination. *Science* **291**, 112-114, doi:10.1126/science.291.5501.112 (2001).
- 79 Fletcher, M.-S. *et al.* Centennial-scale trends in the Southern Annular Mode revealed by hemispheric-wide fire and hydroclimate trends over the past 2400 years. *Geology* **46**, 363-366, doi:10.1130/G39661.1